Inorganic Chemistry

ARTICLE

pubs.acs.org/IC

Geometric and Electronic Structures of Peroxomanganese(III) Complexes Supported by Pentadentate Amino-Pyridine and -Imidazole Ligands

Robert A. Geiger,[†] Domenick F. Leto,[†] Swarup Chattopadhyay,[†,∥] Pierre Dorlet,[‡] Elodie Anxolabéhère-Mallart,*[,§] and Timothy A. Jackson*[,†]

[†]Department of Chemistry and Center for Environmentally Beneficial Catalysis, University of Kansas, Lawrence, Kansas 66045, United States

[‡]Laboratoire Stress Oxydant et Détoxication, CNRS URA 2096 and CEA/iBiTec-S/SB^{2}SM, CEA Saclay, 91191 Gif-sur-Yvette Cedex, France

[§]Laboratoire d'Electrochimie Moléculaire, UMR 7591 CNRS, Université Paris Diderot, Sorbonne Paris Cité, 15 rue Jean-Antoine de Baïf, F-75205 Paris Cedex 13, France

S *Supporting Information*

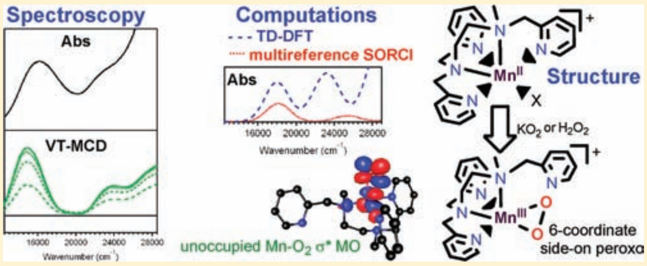

ABSTRACT: Three peroxomanganese(III) complexes $[\mathrm{Mn^{III}(O_2)(mL_5^2)}]^+$, $[\mathrm{Mn^{III}(O_2)(imL_5^2)}]^+$, and $[\mathrm{Mn^{III}(O_2)(N4py)}]^+$ supported by pentadentate ligands ($\mathrm{mL_5^2}$ = *N*-methyl-*N*,*N'*,*N'*-tris(2-pyridylmethyl)ethane-1,2-diamine, $\mathrm{imL_5^2}$ = *N*-methyl-*N*,*N'*,*N'*-tris((1-methyl-4-imidazolyl)methyl)ethane-1,2-diamine, and N4py = *N*,*N*-bis(2-pyridylmethyl)-*N*-bis(2-pyridyl)methylamine) were generated by treating Mn(II) precursors with H_2O_2 or KO_2. Electronic absorption, magnetic circular dichroism (MCD), and variable-temperature, variable-field MCD data demonstrate that these complexes have very similar electronic transition energies and ground-state zero-field splitting parameters, indicative of nearly identical coordination geometries. Because of uncertainty in peroxo (side-on η^2 versus end-on η^1) and ligand (pentadentate versus tetradentate) binding modes, density functional theory (DFT) computations were used to distinguish between three possible structures: pentadentate ligand binding with (i) a side-on peroxo and (ii) an end-on peroxo, and (iii) tetradentate ligand binding with a side-on peroxo. Regardless of the supporting ligand, isomers with a side-on peroxo and the supporting ligand bound in a tetradentate fashion were identified as most stable by >20 kcal/mol. Spectroscopic parameters computed by time-dependent (TD) DFT and multireference SORCI methods provided validation of these isomers on the basis of experimental data. Hexacoordination is thus strongly preferred for peroxomanganese(III) adducts, and dissociation of a pyridine ($\mathrm{mL_5^2}$ and N4py) or imidazole ($\mathrm{imL_5^2}$) arm is thermodynamically favored. In contrast, DFT computations for models of $[\mathrm{Fe^{III}(O_2)(mL_5^2)}]^+$ demonstrate that pyridine dissociation is not favorable; instead a seven-coordinate ferric center is preferred. These different results are attributed to the electronic configurations of the metal centers (high spin d^5 and d^4 for $\mathrm{Fe^{III}}$ and $\mathrm{Mn^{III}}$, respectively), which results in population of a metal-peroxo σ-antibonding molecular orbital and, consequently, longer $\mathrm{M-O_{peroxo}}$ bonds for peroxoiron(III) species.

INTRODUCTION

Mononuclear superoxo- and peroxomanganese(III) species have been proposed to form in a number of redox-active manganese enzymes, including manganese superoxide dismutase (MnSOD),[1−6] manganese-dependent homoprotocatechuate 2,3-dioxygenase (MndD),[7,8] and the oxalate-degrading enzymes oxalate oxidase[9,10] and oxalate decarboxylase.[11−13] In addition, manganese-peroxide interactions are relevant to the dinuclear enzymes manganese catalase[14] and manganese ribonucleotide reductase.[15] Experimental evidence for a peroxomanganese(III) adduct has been obtained for MnSOD. Under high superoxide concentrations, a product-inhibited complex is formed, and this species displays absorption features consistent with a peroxomanganese(III) adduct.[4,6] Notably, the kinetics associated with formation and decay of this intermediate are affected by substitution of outer-sphere amino acid residues.[6,16−19] Rapid freeze-quench electron paramagnetic resonance (EPR) experiments on MndD under single-turnover conditions identified an $S = 5/2$ intermediate with an axial zero-field splitting parameter too large for a $\mathrm{Mn^{II}}$ species (D = 2.5 cm^{-1}).[7] This intermediate was formulated as a superoxomanganese(III) adduct, although a peroxomanganese(III)-(homoprotocatechuate radical) is an alternative possibility.[7] Because these biological peroxo- and superoxomanganese(III) species are highly unstable, relatively little is known concerning their structural, electronic, and reactivity properties.

In contrast, a variety of mononuclear peroxomanganese(III) model complexes have been described (Figure 1),[20−29] and some of

Received: May 31, 2011
Published: August 29, 2011

dx.doi.org/10.1021/ic201168j | *Inorg. Chem.* 2011, 50, 10190–10203

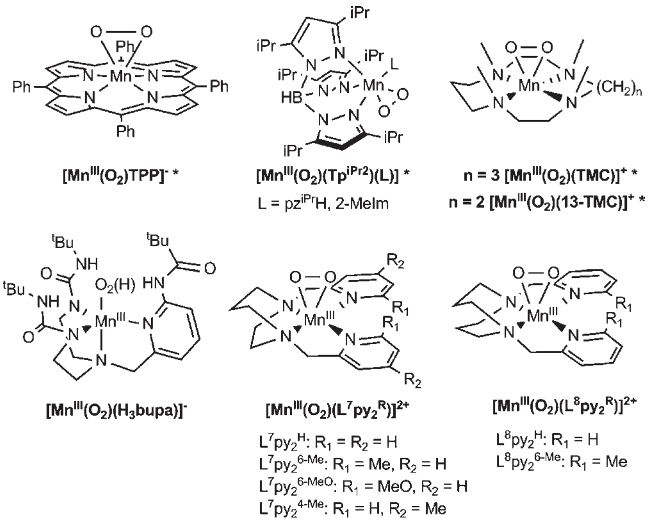

Figure 1. Mononuclear peroxomanganese(III) adducts. Complexes marked with an asterisk have been structurally characterized by X-ray diffraction.

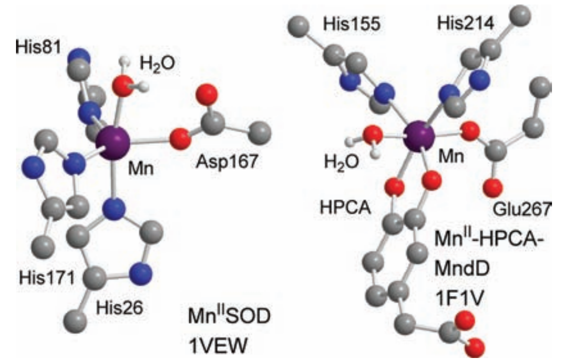

Figure 2. Active sites of Mn^{II}SOD (left) and the HPCA adduct of Mn^{II}MndD (right) derived from PDB files 1VEW and 1F1V, respectively. For clarity, only H-atoms on coordinated solvent ligands are shown.

these have been structurally characterized using X-ray diffraction (XRD). The crystallographically characterized complexes are supported by the dianionic TPP ligand (TPP = *meso*-tetraphenylporphyrin),[20] the monoanionic, facially coordinating Tp^{iPr2} ligand (Tp^{iPr2} = hydrotris(3,5-diisopropylpyrazol-1-yl)-borate),[21,22] and the neutral TMC and 13-TMC ligands (TMC = 1,4,8,11-tetramethyl-1,4,8,11-tetraazacyclotetradecane and 13-TMC = 1,4,7,10-tetramethyl-1,4,7,10-tetraazacyclotridecane).[23,24] Although the properties of these supporting ligands are rather diverse, in all cases the peroxide is bound to the Mn^{III} ions in a side-on (η^2) fashion, and the coordination sphere is completed by four other donors, leading to six-coordinate manganese(III) centers (Figure 1). Nam and co-workers have reported that the Mn^{III} center of the [Mn^{III}(O$_2$)(13-TMC)]$^+$ complex can be bound by exogenous anions X$^-$ (X$^-$ = N$_3$$^-$, NCS$^-$, CN$^-$, and CF$_3CO_2$$^-$).[23] On the basis of the greater nucleophilicity of the resulting [Mn^{III}(O$_2$)(13-TMC)(X)] complexes, they have suggested that anion binding may convert the peroxo from side-on to end-on, thereby retaining a six-coordinate Mn^{III} center.[23] Density functional theory (DFT) computations predict the end-on peroxo ligand to bear significantly more negative charge, in keeping with the increase in nucleophilicity observed experimentally.[23] However, there is no structural data to support this proposal, and, to date, resonance Raman experiments on Mn^{III}–O$_2$ have proved fruitless,[24,26] likely because of photo-induced sample degradation. While the above species were generated using H$_2$O$_2$ or KO$_2$, a peroxomanganese(III) adduct was generated from a Mn^{II} center supported by a dianionic carboxyamidopyridyl-based ligand, [Mn^{II}(H$_3$bupa)] (H$_3$bupa = bis[(*N*′-*tert*-butylureayl)-*N*-ethyl]-(6-pivalamido-2-pyridylmethyl)-amine), using O$_2$ and a sacrificial reductant.[28,30] We have recently reported spectroscopic and theoretical studies of a series of peroxomanganese(III) adducts supported by derivatives of the diazacycloalkane ligand L^{7}py$_2$^{H} (L^{7}py$_2$^{H} = 1,4-bis(2-pyridylmethyl)-1,4-diazepane).[29,31] A major conclusion of one of these studies was that the L^{7}py$_2$$^{6-Me}$ ligand (L^{7}py$_2$$^{6-Me}$ = 1,4-bis(6-methyl-2-pyridylmethyl)-1,4-diazepane), which features pyridines with electron-donating 6-methyl substituents, leads to a more end-on bound peroxo ligand when compared to an analogous compound with the L^{7}py$_2$^{H} ligand.[29] While this spectroscopic and theoretical evidence supports the proposal that the inclusion of electron-rich substituents can lead to peroxo ligands bound in a more end-on fashion, structural information is only available for six-coordinate peroxomanganese(III) adducts with side-on peroxo ligands.

Peroxomanganese(III) adducts with seven-coordination geometries, or with end-on peroxo ligands, could bear greater relevance to analogous enzymatic intermediates. For example, the product-inhibited form of MnSOD is generated by reaction of a five-coordinate Mn^{II} center with superoxide (Figure 2, left). Thus, formation of a side-on peroxomanganese(III) adduct would result in a seven-coordinate Mn^{III} complex, assuming none of the native ligands dissociate. Alternatively, an end-on peroxo ligand would result in a six-coordinate center. A model of the product-inhibited complex of MnSOD developed using DFT computations shows a Mn^{III}–O$_2$ unit with a more end-on structure, with Mn–O$_{peroxo}$ distances of 1.80 and 2.22 Å.[3] The active-site Mn^{II} ion of MndD is bound by three exogenous ligands and reacts with dioxygen in the presence of homoprotocatechuate (HPCA) substrate.[7,8,32] With substrate bound in the expected bidentate fashion and assuming that none of the three proteinaceous ligands dissociate, only one coordination site is available for interaction with oxygen. This site is occupied by water in an X-ray crystal structure (Figure 2, right).[8] Thus, the putative superoxomanganese(III) adduct observed experimentally is likely either an end-on bound six-coordinate species or a side-on bound seven-coordinate species.

In this work we have examined the geometric and electronic structures of peroxomanganese(III) adducts supported by three pentadentate ligands (Scheme 1): mL$_5$^{2} (*N*-methyl-*N*,*N*′,*N*′-tris(2-pyridylmethyl)ethane-1,2-diamine), imL$_5$^{2} (*N*-methyl-*N*,*N*′,*N*′-tris((1-methyl-4-imidazolyl)methyl)ethane-1,2-diamine), and N4py (*N*,*N*-bis(2-pyridylmethyl)-*N*-bis(2-pyridyl)methylamine). Previous spectroscopic and reactivity studies of [Mn^{III}(O$_2$)(mL$_5$^{2})]$^+$ have clearly established the formulation of this species,[26,27] although the coordination geometry of this species is ill-defined (Scheme 1). Results reported herein support the formulation of the new [Mn^{III}(O$_2$)(imL$_5$^{2})]$^+$ and [Mn^{III}(O$_2$)(N4py)]$^+$ complexes. This current study seeks to answer two important questions: Are the peroxomanganese(III) complexes supported by these pentadentate ligands six- or seven-coordinate? If the complexes are six-coordinate, which donor group is dissociating? On the basis of electronic absorption (Abs), magnetic circular dichroism (MCD), variable-temperature, variable-field (VTVH) MCD spectroscopies, as well as density functional

Scheme 1

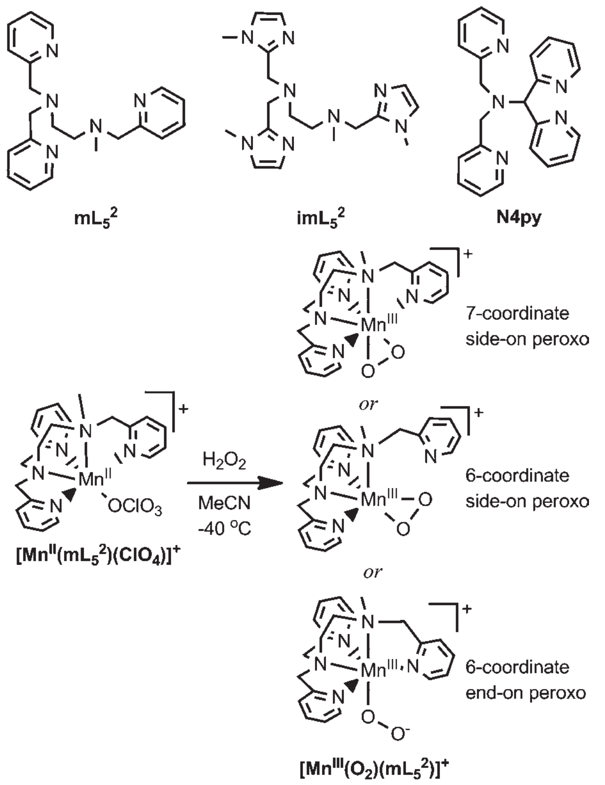

theory (DFT) and multireference ab initio computations, we conclude that all three complexes contain a six-coordinate Mn^{III} center with a side-on peroxo ligand and a dissociated pyridine (or imidazole). Thus, there is a strong preference for six-coordinate geometry for peroxomanganese(III) species, and end-on peroxomanganese(III) units are predicted to be unstable and, potentially, highly reactive. The relevance of these findings with respect to biological manganese centers and corresponding peroxoiron(III) adducts is discussed.

■ MATERIALS AND METHODS

Chemicals and Instrumentation. All chemicals and solvents were obtained from commercial vendors and were ACS grade or better and used as received. ^1H NMR spectra were collected on a Bruker DRZ 400 MHz spectrometer and a Bruker DPX 300 MHz spectrometer with a ONP probe. All ^1H NMR experiments were performed at room temperature in d_1-$CDCl_3$ (δ = 7.24 ppm). Mass spectrometry experiments were performed using an LCT Primers MicroMass electrospray time-of-flight instrument. Elemental analysis for $[Mn^{II}(imL_5^2)(ClO_4)](ClO_4)$ and $[Mn^{II}(N4py)(CF_3SO_3)_2]$ were respectively performed at the Services de Microanalyse, ICSN-CNRS, Gif-sur-Yvette, France, and by Columbia Analytical Services, Tucson AZ. Electronic absorption spectra were obtained on a Varian Cary 50 Bio spectrophotometer that was interfaced with a Unisoku cryostat (USP-203-A) capable of maintaining temperatures between 150 and 373 K. MCD spectra were collected on a Jasco circular dichroism spectrometer (J-815) interfaced with an Oxford Instruments magnetocryostat (SM-4000-8) capable of a horizontal field up to 8 T and a temperature range of 1.5 to 300 K.

Ligand Synthesis. The synthesis of imL_5^2 was adapted from a method previously described in the literature.[33] Changes were made in the synthesis of the preliminary products (1-methylimidazol-2-yl)methanol based on already reported modifications.[34] imL_5^2: 21.75 mL (156 mmol) of triethylamine and 2.25 mL (26 mmol) of *N*-methylethylenediamine were added to a solution of 12 g (78 mmol) of 2-(chloromethyl)-1-methyl-1*H*-imidazole hydrochloride in a mixture of acetonitrile (70 mL) and chloroform (70 mL). The brown mixture was stirred at room temperature for 1 day. The solvents were evaporated and the product was extracted with chloroform (100 mL). The extract was washed with water and dried over $MgSO_4$. After evaporation the resulting brown oil was dried under vacuum. The crude product was purified by flash chromatography (Et_2O/EtOH) to yield the imL_5^2 ligand as a brown oil in 35% yield: ^1H NMR (300 MHz, $CDCl_3$): 7.6 (dd, 6H), 3.65 (s, 4H), 3.35 (s, 3H), 3.25 (s, 2H), 3.18 (s, 6H), 2.45 (t, 2H), 2.18 (t, 2H), 1.75 (s, 3H) ppm. Electrospray ionization-mass spectrometry (ESI-MS) data are as follows: $\{imL_5^2H\}^+$ m/z = 357 (calc. 357).

The synthesis of N4py was performed according to a previously described procedure.[35,36] Di-2-pyridylmethanamine was first synthesized from the reduction of di-2-pyridyl ketone oxime.[35] N4py was then prepared in 40% yield from the reaction of di-2-pyridylmethanamine with 2 equiv of picolyl chloride HCl, followed by treatment with concentrated $HClO_4$ and extraction with dichloromethane.[36] ^1H NMR data (400 MHz) for N4py ($CDCl_3$, δ) 3.97 (s, 4H), 5.35 (s, 1H), 7.13 (m, 4H), 7.63 (m, 8H), 8.51 (d, 2H), 8.57 (d, 2H) ppm.

Preparation of Manganese(II) Complexes. ***Caution!*** *Perchlorate salts of metal complexes with organic ligands are potentially explosive. Only small quantities of these compounds should be prepared, and they should be handled behind suitable protective shields.*

A 103.6 mg portion of $Mn(ClO_4)_2\cdot 6(H_2O)$ (0.29 mmol) in ethanol (2 mL) was added to a solution of imL_5^2 (102 mg, 0.29 mmol) dissolved in ethanol (5 mL). The mixture was stirred, open-air, at room temperature for 2 h. An excess of sodium perchlorate (2.5 equiv) was then added, and the stirring was continued for another 2 h, leading to the formation of a beige precipitate that was collected by filtration, and washed with a minimum of ethanol and diethyl ether (overall yield 70%). Elemental analysis $[Mn^{II}(imL_5^2)ClO_4](ClO_4)\cdot 0.25CH_3CH_2OH$: $C_{18.5}H_{29.5}Cl_2MnN_8O_{8.25}$ calcd (%): C 35.72, H 4.78, N 18.02; found (%): C 35.23, H 4.69, N 17.73. ESI-MS data are as follows: $\{Mn(imL_5^2)\}^{2+}$ m/z = 205.59 (calc. 205.59) and $\{(Mn(imL_5^2)(ClO_4)\}^+$ 510.18 (calc. 510.13).

The $[Mn^{II}(N4py)(OTf)](OTf)$ complex (OTf^- = $CF_3SO_3^-$) was synthesized in excellent yield (~90%) by reacting N4py ligand with $Mn^{II}(OTf)_2$ in acetonitrile (MeCN) solution in a 1:1 molar ratio. $Mn(OTf)_2$ was prepared using a previously reported procedure, where equimolar amounts of $(CH_3)_3Si(OTf)$ and anhydrous $MnCl_2$ are reacted.[24] Details of a representative preparation for a metal complex are as follows. To a stirred solution of 1.84 g (5.223 mmol) of $Mn(OTf)_2$ in 10 mL of MeCN was added N4py (1.92 g, 5.223 mmol) in 10 mL of MeCN. The red solution was stirred overnight and evaporated under reduced pressure. The solid thus obtained was dried in vacuo. Recrystallization of the crude solid from MeCN−diethyl ether afforded nearly colorless crystals of $[Mn^{II}(N4py)(OTf)](OTf)$ (3.27 g, 87%). Elemental analysis $[Mn^{II}(N4py)(OTf)](OTf)\cdot 0.5CH_3CH_2OH$: $MnC_{26}H_{24}N_5O_{6.5}F_6S_2$ calcd (%): C 42.00, H 3.25, N 9.42; found (%): C 42.16, H 3.61, N 9.68. ESI-MS data are as follows: $\{[Mn(N4py)](Cl)^+\}$ m/z = 457.0876 (calc. 457.0866), where a chloride ion was exchanged for a triflate ion in the mass spectrometer.

Preparation of Peroxomanganese(III) Complexes for MCD Experiments. Samples of peroxomanganese(III) complexes supported by the mL_5^2, imL_5^2, and N4py ligands were prepared in glassy solvents for MCD experiments. Unlike the $[Mn^{II}(mL_5^2)](OTf)_2$ salt, $[Mn^{II}(mL_5^2)](BPh_4)_2$ is not soluble in ethanol. The synthesis of $[Mn^{II}(mL_5^2)](BPh_4)_2$ was performed according to a previously published procedure.[37] Accordingly, $[Mn^{III}(O_2)(mL_5^2)]^+$ was prepared by a modification of the reported procedure.[27] A 5 mM frozen solution of $[Mn^{III}(O_2)(mL_5^2)]^+$ was generated by dissolving solid $[Mn^{II}(mL_5^2)](BPh_4)_2$ in a minimal amount of butyronitrile and cooling the resulting solution to −20 °C. Two hundred equivalents of urea-H_2O_2 and a few microliters of H_2O in ethanol were added to the butyronitrile solution. Once formation of $[Mn^{III}(O_2)(mL_5^{2})]^+$ was complete on the basis of electronic absorption data, the solution was passed through a precooled syringe filter to remove undissolved urea. The filtered solution was transferred to an MCD cell and flash-frozen in liquid N_2. A 5 mM frozen solution of $[Mn^{III}(O_2)(imL_5^{2})]^+$ was prepared at −40 °C by adding 10 equiv of H_2O_2 (30% in H_2O) and 10 equiv of triethylamine in ethanol to a 50:50 vol:vol butyronitrile/ethanol solution of $[Mn^{II}(imL_5^{2})(ClO_4)](ClO_4)$. Once formation was judged complete by absorption spectroscopy, the sample was further cooled to −80 °C, transferred to a precooled MCD sample cell at −80 °C, and flash-frozen in liquid N_2. Because of a temperature-dependent shift of the dominant absorption band at ~18 000 cm^{-1} (vide infra), the $[Mn^{III}(O_2)(imL_5^{2})]^+$ sample changes color from purple to blue upon freezing. Two equivalents of KO_2, in the form of a solution prepared from 14.2 mg of KO_2 and 200 mg of 18-crown-6 dissolved in 2 mL of butyronitrile, was added to the 5 mM solution butyronitrile of $[Mn^{II}(N4py)(OTf)_2]$. Once formation of $[Mn^{III}(O_2)(N4py)]^+$ was judged complete by absorption spectroscopy, the sample was further cooled to −80 °C, transferred to a precooled MCD cell at −80 °C, and flash-frozen in liquid N_2.

Computations. All calculations utilized the ORCA 2.8.0 software package developed by F. Neese (University of Bonn, Germany).[38] Crystal structure coordinates of the $[Mn^{II}(mL_5^{2})(ClO_4)_2]$, $[Mn^{II}(imL_5^{2})(ClO_4)](ClO_4)$, and $[Mn^{II}(N4py)(OTf)](OTf)$ complexes were modified to include peroxo ligands and served as the starting points for geometry optimizations. Geometry optimizations and surface scans were performed at the spin-unrestricted level using the Becke−Perdew (BP) functional[39,40] and TZVP (for Mn, O, and N) and SVP (for C and H) basis sets.[41,42] These calculations employed the resolution of the identity (RI) approximation[43] that employed the TZV/J and SV/J auxiliary basis sets.[43] Frequency calculations were used to verify that all energy-minimized models showed no imaginary frequencies. Single-point calculations to obtain energies for the optimized structures employed the B3LYP functional[44−46] and def2-TZVPP basis sets for all atoms.[41,42,47] The effects of acetonitrile solvation on the total energies of these systems were evaluated using the COSMO method as implemented in ORCA. Identical methods were used to obtain optimized structures and total energies for the isomers of the iron complex $[Fe^{III}(O_2)(mL_5^{2})]^+$, with the exception that these computations were converged to the $S = 5/2$ spin state. D-tensor orientations for models of $[Mn^{III}(O_2)(mL_5^{2})]^+$ were computed using a so-called coupled-perturbed spin−orbit coupling approach,[48] which utilized the B3LYP functional and TZVP basis set for all atoms. Isosurface plots of quasi-restricted molecular orbitals (MOs) were generated using the gOpenMol program and the isodensity values of 0.05 au.[49,50] Cartesian coordinates for all geometry optimized models are included in Supporting Information, Tables S1−S13.

Electronic transition energies and intensities were computed for select models using the time-dependent DFT (TD-DFT)[51−54] and spectroscopy oriented configuration interaction (SORCI)[55,56] procedures. TD-DFT calculations were performed within the Tamm−Dancoff approximation and utilized the TZVP (for Mn, N, and O) and SVP (for C and H) basis sets. For each calculations, 40 excited states were calculated by including all one-electron excitations within a ± 3 hartree energy window with respect to the highest occupied and lowest unoccupied MOs. The SORCI calculations used an active space consisting of quasi-restricted Mn 3d-based and peroxo π^*_{ip}- and π^*_{op}-based orbitals (CAS 8,7) obtained from an initial DFT calculation using the level of theory described above. The CI thresholds T_{sel}, T_{pre}, and T_{nat} were set to 10^{-6} hartrees, 10^{-4}, and 10^{-5}, respectively.

■ RESULTS AND ANALYSIS

1.1. Formation and Mass Spectral Characterization of $[Mn^{III}(O_2)(imL_5^{2})]^+$ and $[Mn^{III}(O_2)(N4py)]^+$.

It was previously reported that the $[Mn^{II}(mL_5^{2})]^{2+}$ complex can be converted to the peroxomanganese(III) ($Mn^{III}-O_2$) adduct $[Mn^{III}(O_2)(mL_5^{2})]^+$ by reaction with either KO_2 or H_2O_2.[26,27] The $[Mn^{II}(imL_5^{2})(ClO_4)](ClO_4)$ and $[Mn^{II}(N4py)(OTf)](OTf)$ complexes are structurally similar to $[Mn^{II}(mL_5^{2})(ClO_4)](ClO_4)$, both having the supporting ligands bound in the expected pentadentate fashion, with a counterion (perchlorate and triflate, respectively) completing the coordination sphere.[57] When a 5 mM solution of the $[Mn^{II}(imL_5^{2})(ClO_4)](ClO_4)$ complex is treated with 10 equiv of H_2O_2 and Et_3N in 1:1 butyronitrile/ethanol at −20 °C, the initially colorless solution turns purple within minutes, and the electronic absorption (Abs) spectrum of this solution is very similar to that of $[Mn^{III}(O_2)(mL_5^{2})]^+$ (Figure 3, vide infra). Electrospray ionization mass spectrometry (ESI-MS) experiments on the resulting solution revealed a major ion peak at m/z 443.1697, supporting the assignment of the purple species as $[Mn(O_2)(imL_5^{2})]^+$ (calc. m/z = 443.1716). Similarly, addition of 2 equiv of KO_2 to a 5 mM solution of $[Mn^{II}(N4py)(OTf)](OTf)$ at −40 °C in acetonitrile results in the formation of a blue solution[58] that displays a prominent peak at m/z 454.1097 in an ESI-MS experiment, consistent with its formulation as $[Mn(O_2)(N4py)]^+$ (calc. m/z = 454.1076). As discussed in more detail below, Abs, MCD, and VTVH MCD data collected for these complexes further establish their assignments as peroxomanganese(III) species.

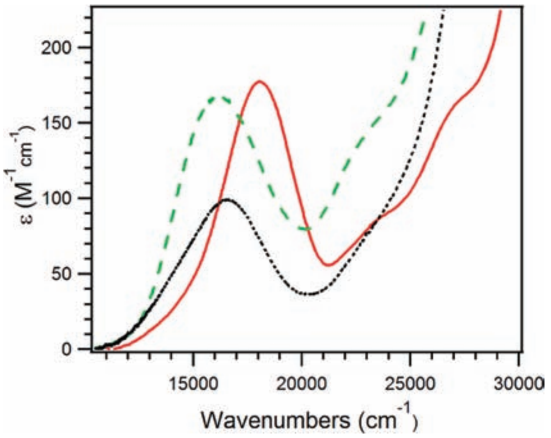

Figure 3. Electronic absorption spectra at 233 K of $[Mn^{III}(O_2)(mL_5^{2})]^+$ (dotted black line), $[Mn^{III}(O_2)(imL_5^{2})]^+$ (solid red line), and $[Mn^{III}(O_2)(N4py)]^+$ (dashed green line).

1.2. Electronic Absorption Spectroscopy.

(A). Comparison of Absorption Spectra. Figure 3 shows an overlay plot of the Abs spectra of the three peroxomanganese(III) complexes, $[Mn^{III}(O_2)(mL_5^{2})]^+$, $[Mn^{III}(O_2)(imL_5^{2})]^+$, and $[Mn^{III}(O_2)(N4py)]^+$. As previously described,[26,27] the Abs spectrum of $[Mn^{III}(O_2)(mL_5^{2})]^+$ displays a prominent band at ~17 200 cm^{-1} and a shoulder at ~23 500 cm^{-1} (ε = 89 and 90 M^{-1} cm^{-1}, respectively).[59] The Abs spectrum of $[Mn^{III}(O_2)(N4py)]^+$ is very similar, with $\lambda_{max} \approx$ 16 200 and 22 800 cm^{-1} (ε = 168 and 139 M^{-1} cm^{-1}, respectively). These similarities suggest common coordination environments for the manganese(III) centers. For all three compounds, no other absorption features are observed down to 9 100 cm^{-1}.

The lowest-energy Abs feature observed for $[Mn^{III}(O_2)(imL_5^{2})]^+$ is at ~18 000 cm^{-1}, and the intensity of this band is roughly twice that of the low-energy band of $[Mn^{III}(O_2)(mL_5^{2})]^+$ but is comparable to that of $[Mn^{III}(O_2)(N4py)]^+$ (Figure 3). Two well-resolved shoulders are observed for $[Mn^{III}(O_2)(imL_5^{2})]^+$ at ~23 200 and 27 000 cm^1. Notably $[Mn^{III}(O_2)(mL_5^{2})]^+$ and

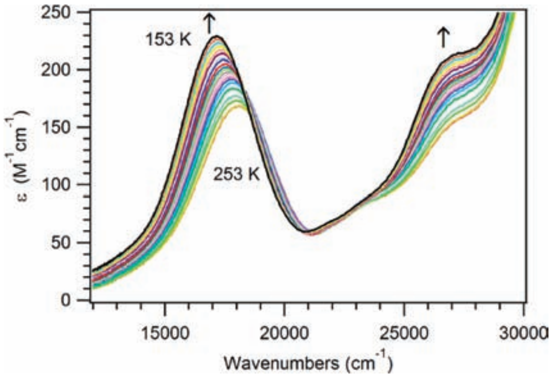

Figure 4. Absorption spectra of $[\mathrm{Mn^{III}(O_2)(imL_5{}^2)}]^+$ from 253 K−153 K collected in 5 K increments.

$[\mathrm{Mn^{III}(O_2)(N4py)}]^+$ show a single shoulder at 23 000 cm^{-1} and the onset of more intense features at >25 000 cm^{-1}. We attribute this difference to the presence of pyridines in the $\mathrm{mL_5{}^2}$ and N4py ligands, which likely give rise to charge-transfer transitions involving π^* pyridine orbitals and intraligand transitions in the near-UV and UV regions that will obscure weaker Abs bands.

(B). Variable-Temperature Absorption Data for $[\mathrm{Mn^{III}(O_2)(imL_5{}^2)}]^+$. As the temperature is decreased from 253 to 153 K, the Abs features of $[\mathrm{Mn^{III}(O_2)(imL_5{}^2)}]^+$ at ~27 000 and 18 000 cm^{-1} gain intensity (Figure 4), and the lower-energy band red-shifts by ~1 500 cm^{-1}. The shoulder at ~23 200 cm^{-1} changes neither energy nor intensity from 253 to 153 K. No isosbestic points are observed. In principle, these spectral perturbations could be due to thermal changes in covalency parameters, associated with a decrease in average metal−ligand bond lengths as temperature is lowered.[60] For metal centered d-d transitions that steal intensity from ligand-to-metal charge transfer transitions, shorter, more covalent metal−ligand bonds promote this intensity-gaining mechanism, leading to an increase in intensity of ligand-field transitions at lower temperatures. However, this behavior is usually associated with slight blue-shifts of electronic transition energies and uniform changes for all absorption features, and this is not observed for $[\mathrm{Mn^{III}(O_2)(imL_5{}^2)}]^+$ (Figure 4). The fact that only two of the visible bands respond fairly dramatically to a 100 K change in temperature suggests a specific, temperature-dependent structural perturbation may be occurring. Insights into the potential origin of the thermal transition for $[\mathrm{Mn^{III}(O_2)(imL_5{}^2)}]^+$ come from the $[\mathrm{Mn^{III}(O_2)(Tp^{iPr})(pz^{iPr}H)}]^+$ ($\mathrm{pz^{iPr}H}$ = 3,5-diisopropylpyrazole) complex, where blue ($\lambda_{\max}$ = 17 150 cm^{-1}) and brown ($\lambda_{\max}$ = 17 800 cm^{-1}) isomers are formed at 195 and 253 K, respectively.[21] X-ray crystal structures of these isomers revealed an intramolecular hydrogen-bond between the $\mathrm{pz^{iPr}H}$ and peroxo ligands in the blue form that gives rise to asymmetric Mn−O distances of 1.841 and 1.878 Å. In contrast, the brown isomer lacks this hydrogen-bond and displays symmetric Mn−O distances of 1.850 and 1.851 Å.[21] Because H_2O_2 in EtOH is added to the butyronitrile solution of $[\mathrm{Mn^{III}(O_2)(imL_5{}^2)}]^+$, it is possible that intermolecular H-bonding between the peroxo ligand in $[\mathrm{Mn^{III}(O_2)(imL_5{}^2)}]^+$ and EtOH could be responsible for the thermochromic behavior of this complex. Alternatively, as described in more detail below (see section 2.3), DFT computations for a model of $[\mathrm{Mn^{III}(O_2)(imL_5{}^2)}]^+$ show that shortening a Mn−N(amine) bond length by 0.30 Å causes an energy increase of only 2.6 kcal/mol and is associated with a red-shift of the lowest energy absorption feature. As this Mn−N(amine) bond is *trans* to the peroxo unit (vide infra), these two structural perturbations could be related.

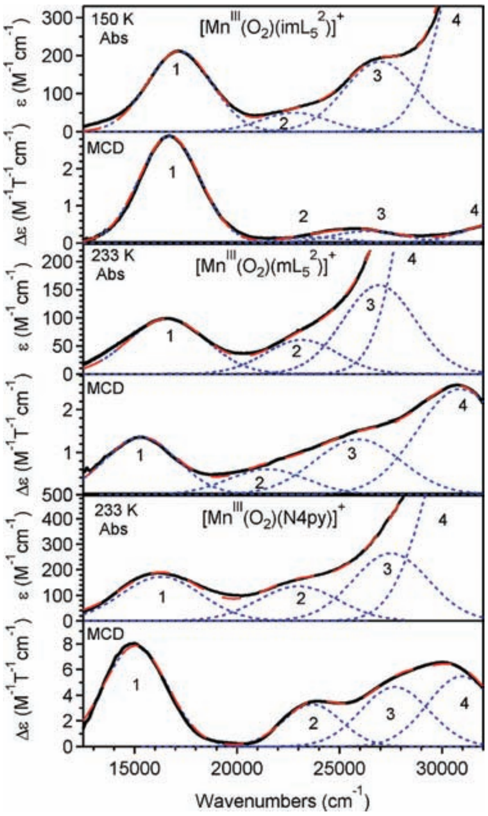

Figure 5. Abs and 4.5 K, 7 T MCD spectra of $[\mathrm{Mn^{III}(O_2)(imL_5{}^2)}]^+$ (top two panels), $[\mathrm{Mn^{III}(O_2)(mL_5{}^2)}]^+$ (middle two panels), and $[\mathrm{Mn^{III}(O_2)(N4py)}]^+$ (bottom two panels). Individual transitions (blue dotted lines) and their sums (red dashed lines) obtained from an iterative Gaussian fit of the data sets, are displayed on their respective spectra. Complete fit parameters are included in the Supporting Information. Conditions: Abs data for $[\mathrm{Mn^{III}(O_2)(mL_5{}^2)}]^+$ (233 K) and $[\mathrm{Mn^{III}(O_2)(N4py)}]^+$ (233 K) from MeCN solutions. Corresponding data for $[\mathrm{Mn^{III}(O_2)(imL_5{}^2)}]^+$ was collected for a frozen solution of butyronitrile/ethanol at 150 K. MCD data for $[\mathrm{Mn^{III}(O_2)(mL_5{}^2)}]^+$ and $[\mathrm{Mn^{III}(O_2)(N4py)}]^+$ were collected for frozen butyronitrile solutions; MCD data for $[\mathrm{Mn^{III}(O_2)(imL_5{}^2)}]^+$ was of a 50:50 vol:vol ethanol/butyronitrile mixture.

1.3. MCD Spectroscopy and Spectral Deconvolution. To compare the $[\mathrm{Mn^{III}(O_2)(mL_5{}^2)}]^+$, $[\mathrm{Mn^{III}(O_2)(imL_5{}^2)}]^+$, and $[\mathrm{Mn^{III}(O_2)(N4py)}]^+$ complexes in more detail, low-temperature magnetic circular dichroism (MCD) data were collected (Figure 5). For all complexes, the intensities of the MCD features between 11 000 and 34 000 cm^{-1} show an inverse temperature dependence (*C*-term behavior), consistent with the paramagnetic ground states of these compounds. The MCD spectrum of $[\mathrm{Mn^{III}(O_2)(imL_5{}^2)}]^+$ is considerably simpler than that of $[\mathrm{Mn^{III}(O_2)(mL_5{}^2)}]^+$ and $[\mathrm{Mn^{III}(O_2)(N4py)}]^+$, showing only three maxima (Figure 5). We attribute this to the lack of pyridines in the $\mathrm{imL_5{}^2}$ ligand, which results in fewer excited states with energies in the visible to near-UV region.

Iterative Gaussian deconvolutions of the Abs and MCD data shown in Figure 5 were performed to determine the minimum number of electronic transitions responsible for the spectral features of $[\mathrm{Mn^{III}(O_2)(mL_5{}^2)}]^+$, $[\mathrm{Mn^{III}(O_2)(imL_5{}^2)}]^+$, and $[\mathrm{Mn^{III}(O_2)(N4py)}]^+$. Because the Abs and MCD data were collected at different temperatures, the positions of the Gaussian bands were

Table 1. Energies ($\mathrm{cm^{-1}}$) and Oscillator Strengths ($f_{\mathrm{exp}} \times 10^3$) of Electronic Transitions for $[\mathrm{Mn^{III}(O_2)(imL_5{}^2)}]^+$, $[\mathrm{Mn^{III}(O_2)(mL_5{}^2)}]^+$, and $[\mathrm{Mn^{III}(O_2)(N4py)}]^+$ Obtained from Gaussian Deconvolution of Experimental Absorption and MCD Spectra

	$[\mathrm{Mn^{III}(O_2)(imL_5{}^2)}]^+$			$[\mathrm{Mn^{III}(O_2)(mL_5{}^2)}]^+$			$[\mathrm{Mn^{III}(O_2)(N4py)}]^+$	
band	energy	$f_{\mathrm{exp}} \times 10^3$	band	energy	$f_{\mathrm{exp}} \times 10^3$	band	energy	$f_{\mathrm{exp}} \times 10^3$
1	Abs: 17 200	3.58	1	Abs: 16 600	2.03	1	Abs: 16300	3.64
	MCD: 16 720			MCD: 15 325			MCD: 15064	
2	Abs: 22 800	0.883	2	Abs: 23 155	1.25	2	Abs: 23000	2.85
	MCD: 23 800			MCD: 21 500			MCD: 23670	
3	Abs: 27 000	3.53	3	Abs: 26 940	3.02	3	Abs: 27510	5.28
	MCD: 26 400			MCD: 25 900			MCD: 27710	
4	Abs: 32 200	13.8	4	Abs: 30 770	20.20	4	Abs: 31044	16.38
	MCD: 32 800			MCD: 30 900			MCD: 30960	

allowed to shift by up to 1 500 $\mathrm{cm^{-1}}$, but in most cases shifts were significantly smaller. The energies obtained from deconvolution of these data sets are collected in Table 1, along with oscillator strengths for the Abs bands. Complete information regarding Abs and MCD deconvolution are in the Supporting Information, Table S14. Because of the apparent simplicity of the Abs and MCD data for $[\mathrm{Mn^{III}(O_2)(imL_5{}^2)}]^+$, the spectral analysis of this complex will be discussed first.

(A). $[\mathrm{Mn^{III}(O_2)(imL_5{}^2)}]^+$. Spectral deconvolution for $[\mathrm{Mn^{III}(O_2)(imL_5{}^2)}]^+$ reveals at least four bands from 13 000 to 33 000 $\mathrm{cm^{-1}}$. Band 1 gives rise to the prominent Abs and MCD feature at ~16 700 $\mathrm{cm^{-1}}$, that shows a strong blue-shift as temperature is increased (Figure 4). Bands 2 and 3 are responsible for the other two Abs features at ~23 200 and 27 000 $\mathrm{cm^{-1}}$, and contribute to a weak MCD feature centered at ~26 000 $\mathrm{cm^{-1}}$. Band 4 accounts in part for the rising Abs intensity at ~30 000 $\mathrm{cm^{-1}}$, but is responsible for a weak MCD feature. Because of the expected low symmetry of the $\mathrm{Mn^{III}}$ center in $[\mathrm{Mn^{III}(O_2)(imL_5{}^2)}]^+$, four d-d transitions are anticipated for this high-spin d^4 metal. Band 1 is the lowest energy feature observed for $[\mathrm{Mn^{III}(O_2)(imL_5{}^2)}]^+$, and, considering its relatively large MCD intensity as well as its temperature-dependent Abs intensity, this band is assigned as the lowest energy d-d transition, which, using symmetry labels of the parent octahedral point group, involves excitation within the ${}^5E_g$ ground state that is split in the low-symmetry ligand field. For this d^4 system, the transition corresponds to a one-electron excitation within the e_g-derived orbitals. For peroxomanganese(III) complexes, the splitting of these orbitals arises because of the stronger σ-interactions with the peroxo ligands relative to the N-donor ligands.[29] The low oscillator strengths of bands 2 and 3 (Table 1) lead us to tentatively attribute these bands to $\mathrm{Mn^{III}}$ d-d transitions as well, although these transitions, especially band 2 which carries almost negligible MCD intensity, could also be weak peroxo-to-manganese(III) charge-transfer (CT) bands.[29] Given its considerably larger Abs intensity, band 4 is assigned as a peroxo-to-manganese(III) CT transition.

(B). $[\mathrm{Mn^{III}(O_2)(mL_5{}^2)}]^+$ and $[\mathrm{Mn^{III}(O_2)(N4py)}]^+$. The Abs and MCD spectra of $[\mathrm{Mn^{III}(O_2)(mL_5{}^2)}]^+$ and $[\mathrm{Mn^{III}(O_2)(N4py)}]^+$ are both well fit with a minimum of four Gaussian bands between 12 000 and 32 000 $\mathrm{cm^{-1}}$ (Figure 5). In most cases, the energies of these bands are within ~2 000 $\mathrm{cm^{-1}}$ to those of $[\mathrm{Mn^{III}(O_2)(imL_5{}^2)}]^+$ (Table 1), firmly establishing the geometric and electronic similarities of these complexes. Thus, the tentative band assignments discussed above for $[\mathrm{Mn^{III}(O_2)(imL_5{}^2)}]^+$ are expected to apply to the $[\mathrm{Mn^{III}(O_2)(mL_5{}^2)}]^+$ and $[\mathrm{Mn^{III}(O_2)(N4py)}]^+$ complexes as well. Overall, the Gaussian analyses of Abs and MCD data collected for these three peroxomanganese(III) adducts provide strong evidence that the $\mathrm{Mn^{III}}$ centers in these three complexes share a common geometry.

1.4. VTVH MCD Spectroscopy. Variable-temperature, variable-field (VTVH) MCD spectroscopy was used to determine ground-state zero-field splitting (ZFS) parameters and transition polarizations for the three peroxomanganese(III) complexes. In these experiments, the intensity of an MCD signal at a given wavelength is monitored as a function of magnetic field at various fixed temperatures. For $S > 1/2$ systems, the saturation behavior of these curves reflect the ground-state g-values and axial (D) and rhombic (E/D) ZFS parameters as well as transition polarization.[61,62] VTVH MCD curves collected at several wavelengths for the same sample are thus useful for evaluating the polarizations of different transitions. For example, VTVH MCD data collected for bands 1 and 4 of $[\mathrm{Mn^{III}(O_2)(mL_5{}^2)}]^+$ (16 700 and 30 800 $\mathrm{cm^{-1}}$) show distinct saturation behavior (Figure 6, A and B), with the MCD signal saturating more rapidly for band 1. Fits of these data sets using ZFS parameters and g-values obtained by EPR experiments ($g_{\mathrm{iso}} = 2.0$, $D = -2.9$ $\mathrm{cm^{-1}}$ and $E/D = 0.075$)[27] reveal that band 1 is predominantly y-polarized with a minor x-component (5% x-, 89% y-, and 6% z-polarization), whereas band 4 is nearly 100% z-polarized (<1% x, <1% y-, and 99% z-polarization). VTVH MCD data collected for band 3 (26 700 $\mathrm{cm^{-1}}$) appear almost identical to those of band 4, indicating that this band is also z-polarized (Supporting Information, Figure S2 and Table S15).

Because ZFS parameters have not been previously determined for $[\mathrm{Mn^{III}(O_2)(imL_5{}^2)}]^+$ and $[\mathrm{Mn^{III}(O_2)(N4py)}]^+$, VTVH MCD data for these complexes were systematically fit to extract both ZFS parameters and transition polarizations. In this protocol, D and E/D were respectively varied from -3 to 3 $\mathrm{cm^{-1}}$ and 0 to 0.3 in increments of 0.5 and 0.05 $\mathrm{cm^{-1}}$.[3] Transition-moment products were optimized to fit the experimental data for a given set of D and E/D values. The goodness of fit was assessed by the χ^2 value, which is the sum of the squares of the differences between experimental and fit data sets. All data sets were best fit assuming an $S = 2$ ground state. To evaluate the accuracy of this protocol in determining ZFS parameters for these peroxomanganese(III) complexes, it was first applied to $[\mathrm{Mn^{III}(O_2)(mL_5{}^2)}]^+$. Supporting Information, Figure S3 shows contours plots of χ^2 as a function of D and E/D for VTVH MCD data collected at bands 3 and 4 (26 000 and 30 800 $\mathrm{cm^{-1}}$, respectively). In both cases, excellent fits are obtained for $|D| = 2.5-3$ $\mathrm{cm^{-1}}$ and $E/D = 0.05-0.30$. Thus, for this system, the goodness of fit is strongly

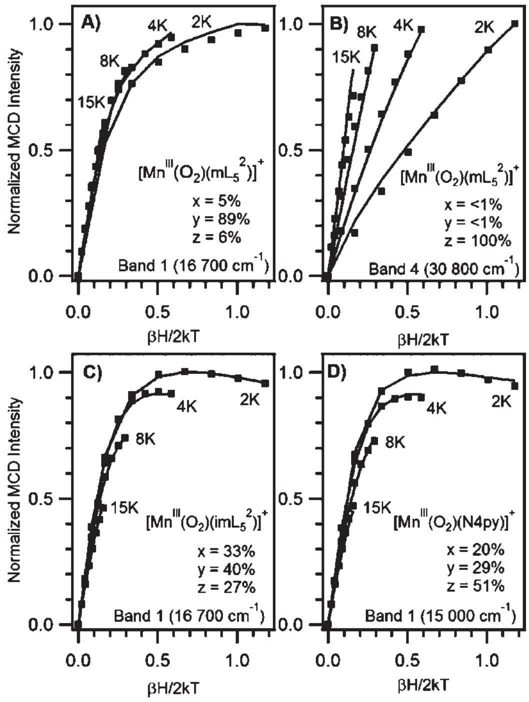

Figure 6. VTVH MCD data (dots) collected for $[\mathrm{Mn^{III}(O_2)(mL_5^2)}]^+$ (A and B), $[\mathrm{Mn^{III}(O_2)(imL_5^2)}]^+$ (C), and $[\mathrm{Mn^{III}(O_2)(N4py)}]^+$ (D) at the energies indicted in the insets. Fits (solid lines) of these data sets used $g_{\mathrm{iso}} = 2.0$, the polarizations listed in the insets, and the following ZFS parameters: $[\mathrm{Mn^{III}(O_2)(mL_5^2)}]^+$, $D = -2.9$ cm^{-1}, $E/D = 0.075$; $[\mathrm{Mn^{III}(O_2)(imL_5^2)}]^+$, $D = -2$ cm^{-1}, $E/D = 0.3$; $[\mathrm{Mn^{III}(O_2)(N4py)}]^+$, $D = -1.5$ cm^{-1}, $E/D = 0.25$.

dependent on the magnitude of D, but insensitive to the sign of D and to the rhombicity. Importantly, the ZFS parameters determined by EPR spectroscopy ($D = -2.9$ cm^{-1} and $E/D = 0.075$) fall within this range.[26,27] We thus conclude that this protocol will yield accurate values for the magnitude of D for $[\mathrm{Mn^{III}(O_2)(imL_5^2)}]^+$ and $[\mathrm{Mn^{III}(O_2)(N4py)}]^+$.

VTVH MCD data collected for $[\mathrm{Mn^{III}(O_2)(imL_5^2)}]^+$ at 16 700 cm^{-1} (Figure 6C) were well fit ($\chi^2 < 0.02$) within the two ranges $D = -1.5$ to -2 cm^{-1}, $E/D = 0.1-0.3$ and $D = +2$, $E/D = 0.1-0.25$ (Supporting Information, Figure S4, left). However, the acceptable range for $D < 0$ cm^{-1} can be narrowed to $D = -2$ cm^{-1}, $E/D = 0.25-0.30$ when data collected at 25 600 cm^{-1} are also considered (Supporting Information, Figure S4, right). Likewise, data collected for $[\mathrm{Mn^{III}(O_2)(N4py)}]^+$ at 14 700 cm^{-1} (Figure 6D) are well fit with $D = -1.5$ cm^{-1}, $E/D = 0.15-0.30$ and $D = +1.5$ to $+2.0$ cm^{-1}, $E/D = 0-0.33$ (Supporting Information, Figure S5).[63] Thus, in both cases the magnitude of D is reduced relative to that of $[\mathrm{Mn^{III}(O_2)(mL_5^2)}]^+$, but the sign of D cannot be unambiguously assigned. Given the strong similarities between the absorption and the MCD data of these three complexes, as well as the fact that all ZFS parameters determined for peroxomanganese(III) adducts to date show $D < 0$,[26−29] we conclude that $[\mathrm{Mn^{III}(O_2)(imL_5^2)}]^+$ and $[\mathrm{Mn^{III}(O_2)(N4py)}]^+$ likewise have negative D values (Table 2). Under this assumption, and using ZFS parameters giving optimal χ^2 values, transition polarizations were determined for the different MCD features of $[\mathrm{Mn^{III}(O_2)(imL_5^2)}]^+$ and $[\mathrm{Mn^{III}(O_2)(N4py)}]^+$ (Supporting Information, Table S15).

Table 2. Axial (D) and Rhombic (E/D) Zero-Field Splitting Parameters for Peroxomanganese(III) Complexes

	D (cm^{-1})	E/D	reference
$[\mathrm{Mn^{III}(O_2)(mL_5^2)}]^+$	−2.9	0.075	26,27
$[\mathrm{Mn^{III}(O_2)(imL_5^2)}]^+$	−2.0	0.25−0.30	*a*
$[\mathrm{Mn^{III}(O_2)(N4py)}]^+$	−1.5	0.15−0.30	*a*
$[\mathrm{Mn^{III}(O_2)(L^7py_2^{H})}]^{+b}$	−2	0.13	29
$[\mathrm{Mn^{III}(O_2)(L^7py_2^{Me})}]^{+c}$	−3	0.05	29
$[\mathrm{Mn^{III}(O_2)(H_3bupa)}]^{-d}$	−2.0	0.13	28

[a] This work.

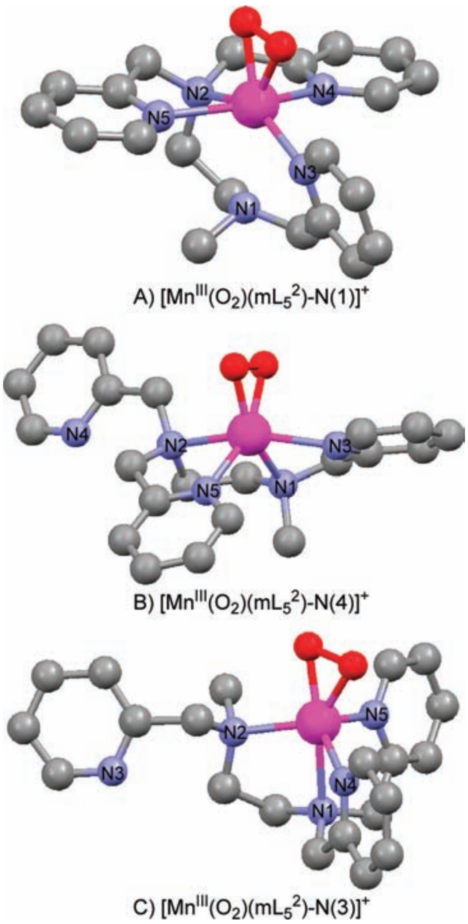

A) $[\mathrm{Mn^{III}(O_2)(mL_5^2)\text{-}N(1)}]^+$

B) $[\mathrm{Mn^{III}(O_2)(mL_5^2)\text{-}N(4)}]^+$

C) $[\mathrm{Mn^{III}(O_2)(mL_5^2)\text{-}N(3)}]^+$

Figure 7. Hypothetical structures of $[\mathrm{Mn^{III}(O_2)(mL_5^2)}]^+$ complexes developed using DFT computations.

Taken together, the results of the MCD and VTVH MCD experiments reveal that the ground- and excited-state properties of these complexes compare favorably with one another, which requires that these three complexes have very similar coordination geometries. Importantly, these spectroscopic data can also provide a basis for evaluating a variety of hypothetical models developed using DFT computations through comparison of computed and experimental spectroscopic parameters.

2. Density Functional Theory Computations. *2.1. Hypothetical Structures for $[\mathrm{Mn^{III}(O_2)(mL_5^2)}]^+$.* Several structures were considered as hypothetical models of $[\mathrm{Mn^{III}(O_2)(mL_5^2)}]^+$ (Scheme 1): (i) a seven-coordinate $\mathrm{Mn^{III}}$ center with a side-on

Table 3. Relative Energies (kcal/mol) and Mn−Ligand Bond Lengths (Å) for Four Hypothetical Models of $[Mn^{III}(O_2)(mL_5^{2})]^+$, $[Mn^{III}(O_2)(imL_5^{2})]^+$, and $[Mn^{III}(O_2)(N4py)]^+$ Developed using DFT Computations

	relative energy	Mn−O	O−O	Mn−N(1)	Mn−N(2)	Mn−N(3)	Mn−N(4)	Mn−N(5)
$[Mn^{III}(O_2)(mL_5^{2})$-N(1)$]^+$	17.9	1.899	1.427	2.610	2.349	2.187	2.275	2.272
	19.3[a]	1.894						
	21.3[b]							
$[Mn^{III}(O_2)(mL_5^{2})$-N(4)$]^+$	0	1.850	1.433	2.204	2.368	2.285	5.209	2.095
	0[a]	1.848						
	0[b]							
$[Mn^{III}(O_2)(mL_5^{2})$-N(3)$]^+$	6.5	1.873	1.422	2.444	2.226	5.137	2.167	2.244
	7.6[a]	1.864						
	8.0[b]							
$[Mn^{III}(O_2)(imL_5^{2})$-N(1)$]^+$	20.3	1.873	1.420	2.805	2.529	2.096	2.240	2.236
	21.4[a]	1.869						
$[Mn^{III}(O_2)(imL_5^{2})$-N(4)$]^+$	8.4	1.861	1.434	2.240	2.447	2.247	5.345	2.067
	9.2[a]	1.847						
$[Mn^{III}(O_2)(imL_5^{2})$-N(3)$]^+$	0	1.860	1.431	2.723	2.359	5.408	2.088	2.088
	0[a]	1.857						
$[Mn^{III}(O_2)(N4py)$-N(1)$]^+$	24.9	1.870	1.417	2.510	2.274	2.240	2.293	2.278
	26.6[a]	1.862						
$[Mn^{III}(O_2)(N4py)$-N(2)$]^+$	0	1.869	1.425	2.419	5.335	2.209	2.076	2.206
	0[a]	1.845						
$[Mn^{III}(O_2)(N4py)$-N(3)$]^+$	6.5	1.867	1.421	2.453	2.230	5.078	2.166	2.126
	4.6[a]	1.862						

[a] The total-energy calculated for gas-phase optimized geometry included solvation effects associated with acetonitrile that were incorporated using the COSMO method. [b] Both the geometry optimization and the total-energy calculations included acetonitrile solvation effects using COSMO.

peroxo ligand and mL_5^{2} bound in a pentadentate fashion, (ii) a six-coordinate complex with an end-on peroxo ligand and mL_5^{2} bound in a pentadentate fashion, and (iii) a six-coordinate complex with a side-on peroxo ligand and mL_5^{2} bound in a tetradentate fashion (i.e., with a dissociated amine or pyridine group). Notably, dissociation of a pyridine arm for mL_5^{2} was previously observed in the X-ray crystal structure of $[Fe_2(\mu\text{-}O)(Cl)_2(mL_5^{2})_2](NEt_4)_2$.[64] Two recently crystallized bis(μ-oxo)dimanganese(IV,IV) species supported by ligands similar to mL_5^{2}, but with a carboxylate replacing one of the pyridine groups (bpmg and mcbpen),[65] also showed dissociation of a pyridine arm.[66] We first examined the possibility of side-on versus end-on peroxo coordination with the mL_5^{2} ligand bound in its commonly observed pentadentate binding mode. Starting geometries were obtained by modifying the crystal structure coordinates of $[Mn^{II}(mL_5^{2})(ClO_4)]^+$ by replacing perchlorate with a peroxo ligand in either a side-on or end-on geometry. In both cases, these starting geometries yielded the same structure upon convergence (referred to as $[Mn^{III}(O_2)(mL_5^{2})$-N(1)$]^+$; see Figure 7): a side-on Mn^{III}−O_2 adduct with Mn−O_{peroxo} distances of 1.899 and 1.894 Å (Table 3). In this structure, the amine nitrogen *trans* to the peroxo unit, N(1), displays a long Mn−N(1) distance of 2.61 Å. To evaluate the energetic and structural consequences associated with conversion from the $[Mn^{III}(O_2)(mL_5^{2})$-N(1)$]^+$ geometry to a Mn^{III}−O_2 complex with an end-on peroxo, we performed a relaxed surface scan where one Mn−O_{peroxo} distance was elongated from 1.85 to 2.60 Å in 0.1 Å increments. As shown in Supporting Information, Figure S6 (top), elongation of the Mn−O_{peroxo} distance leads to a substantial increase in energy, indicating that the side-on peroxo binding mode is strongly favored. The O−O bond length decreases from 1.413 to 1.363 Å as one Mn−O_{peroxo} distance is elongated (Supporting Information, Figure S6, center). The shortest O−O distance is midway between common ranges observed for peroxo and superoxo ligands (1.50−1.40 and 1.30−1.20 Å, respectively). Notably the elongation in one Mn−O_{peroxo} distance is associated with a shortening of the Mn−N(1) bond length by 0.3 Å over the course of the surface scan (Supporting Information, Figure S6, bottom). A complementary surface scan of Mn−N(1) distance showed a similar inverse correlation between the Mn−N(1) distance and one Mn−O_{peroxo} bond length (Supporting Information, Figure S7), which is taken to indicate the preference for hexacoordination for the Mn^{III} center. In either case, elongation of one Mn−O_{peroxo} bond by more than ∼0.3 Å results in models with significantly higher energies (>7 kcal/mol) relative to $[Mn^{III}(O_2)(mL_5^{2})$-N(1)$]^+$.

Given the clear preference for both side-on peroxo binding and a six-coordinate Mn^{III} center, we next evaluated the possibility of dissociation of one of the pyridine arms of mL_5^{2} through two relaxed surface scans. In these calculations the Mn−N(4) and Mn−N(3) distances (see Figure 7 for atom labeling) were elongated through rotation of the appropriate pyridylmethyl arms. In both scans, local minima were found that correspond to six-coordinate complexes with side-on peroxo ligands and dissociated pyridines. These structures were subjected to full geometry optimization, with no structural parameters fixed, to provide an even comparison with $[Mn^{III}(O_2)(mL_5^{2})$-N(1)$]^+$. These fully optimized structures, referred to as $[Mn^{III}(O_2)(mL_5^{2})$-N(3)$]^+$ and $[Mn^{III}(O_2)(mL_5^{2})$-N(4)$]^+$ for dissociated

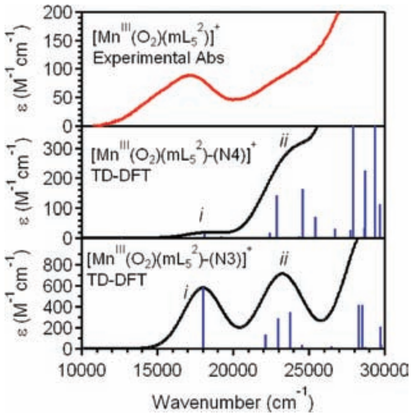

Figure 8. Experimental electronic absorption spectrum of $[Mn^{III}(O_2)(mL_5^2)]^+$ (top) and TD-DFT-computed absorption spectra for $[Mn^{III}(O_2)(mL_5^2)\text{-N(4)}]^+$ (center) and $[Mn^{III}(O_2)(mL_5^2)\text{-N(3)}]^+$ (bottom). The vertical sticks represent individual electronic transitions.

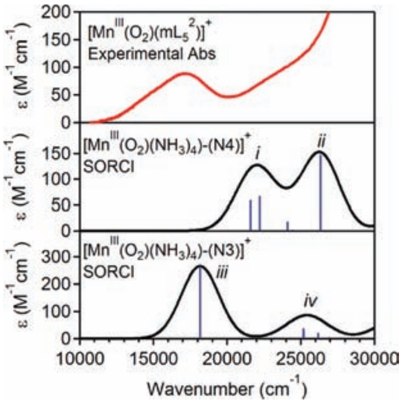

Figure 9. Experimental electronic absorption spectrum of $[Mn^{III}(O_2)(mL_5^2)]^+$ (top) and SORCI-computed absorption spectra for $[Mn^{III}(O_2)(NH_3)_4\text{-N(4)}]^+$ (center) and $[Mn^{III}(O_2)(NH_3)_4\text{N(3)}]^+$ (bottom).

N(3) and N(4) atoms, respectively, are lower in energy than $[Mn^{III}(O_2)(mL_5^2)\text{-N(1)}]^+$ by ∼20 and 14 kcal/mol (Table 3). Thus, pyridine dissociation is strongly favored for $[Mn^{III}(O_2)(mL_5^2)]^+$. The relative energies show a very small dependence on solvation effects, which were incorporated using the COSMO method (Table 3). Given the expected accuracy of total energies obtained by B3LYP DFT calculations for transition metal systems (∼5 kcal/mol),[67] both $[Mn^{III}(O_2)(mL_5^2)\text{-N(4)}]^+$ and $[Mn^{III}(O_2)(mL_5^2)\text{-N(3)}]^+$ appear to be reasonable models.

The optimized structures of $[Mn^{III}(O_2)(mL_5^2)\text{-N(4)}]^+$ and $[Mn^{III}(O_2)(mL_5^2)\text{-N(3)}]^+$ reveal the coordinative flexibility of the mL_5^2 ligand (Figure 7 and Table 3). The Mn^{III} center of $[Mn^{III}(O_2)(mL_5^2)\text{-N(4)}]^+$ is in a distorted octahedral geometry, with N(2)−Mn−N(3) and N(1)−Mn−N(5) angles of 156° and 101°. With regards to the Mn^{III} coordination geometry, $[Mn^{III}(O_2)(mL_5^2)\text{-N(4)}]^+$ is very similar to the XRD structures of $[Mn^{III}(O_2)(TMC)]^+$ and $[Mn^{III}(O_2)(13\text{-TMC})]^+$,[23,24] as well as the DFT-computed structures of $[Mn^{III}(O_2)(L^7py_2^R)]^+$ complexes (Figure 1).[29,31] In all these structures, the peroxo sits above four nitrogen atoms in a tetragonal arrangement. In contrast, the N ligands in $[Mn^{III}(O_2)(mL_5^2)\text{-N(3)}]^+$ are bound in a tripodal fashion, with N(1) occupying the basal position and N(2), N(4), and N(5) defining a trigonal plane. In this case, the coordination geometry around the Mn^{III} center is very similar to that proposed for $[Mn^{III}(O_2)(H_2bupa)]^-$, although the latter complex contains a dianionic ligand and likely possesses second-sphere H-bonding interactions with the peroxo moiety (Figure 1).[28,30]

2.2. Spectroscopic Properties of $[Mn^{III}(O_2)(mL_5^2)\text{-N(4)}]^+$ and $[Mn^{III}(O_2)(mL_5^2)\text{-N(3)}]^+$. To evaluate the validity of the $[Mn^{III}(O_2)(mL_5^2)\text{-N(4)}]^+$ and $[Mn^{III}(O_2)(mL_5^2)\text{-N(3)}]^+$ models, the TD-DFT method was used to determine electronic transition energies and oscillator strengths. The Abs spectra obtained from these computations are shown in Figure 8, and the experimental spectrum is included for comparison. The TD-DFT-computed Abs spectra of $[Mn^{III}(O_2)(mL_5^2)\text{-N(4)}]^+$ and $[Mn^{III}(O_2)(mL_5^2)\text{-N(3)}]^+$ both contain sets of bands at ∼18 000 and 23 500 cm^{-1} (bands *i* and *ii*) that are in good agreement with the experimental Abs spectrum of $[Mn^{III}(O_2)(mL_5^2)]^+$, which shows a band at ∼17 300 cm^{-1}, a shoulder at ∼23 500 cm^{-1}, and more intense features at higher energy. However, the intensity ratios of bands *i* and *ii* are dramatically different for $[Mn^{III}(O_2)(mL_5^2)\text{-N(4)}]^+$ and $[Mn^{III}(O_2)(mL_5^2)\text{-N(3)}]^+$ (0.06:1 and 0.80:1, respectively). Only the latter is in reasonable agreement with the ∼1:1 ratio of experimental Abs intensities at 15 000 and 26 000 cm^{-1}. Band *i* of $[Mn^{III}(O_2)(mL_5^2)\text{-N(3)}]^+$ is predominantly *y*-polarized with a slight *x*-component (14% *x*-, 85% *y*-, and <1% *z*-polarization), in excellent agreement with analysis of VTVH MCD data collected for band 1 (5% *x*-, 89% *y*-, and 6% *z*-polarization; see Figure 6).[68] In contrast, band *i* of $[Mn^{III}(O_2)(mL_5^2)\text{-N(4)}]^+$ is significantly more *z*-polarized (4% *x*-, 67% *y*-, and 29% *z*-polarization), inconsistent with experimental data. On the basis of the agreement between experimental and TD-DFT-computed electronic transition energies, oscillator strengths, and polarizations $[Mn^{III}(O_2)(mL_5^2)\text{-N(3)}]^+$ is a better model for $[Mn^{III}(O_2)(mL_5^2)]^+$.

To ensure that our selection of $[Mn^{III}(O_2)(mL_5^2)\text{-N(3)}]^+$ over $[Mn^{III}(O_2)(mL_5^2)\text{-N(4)}]^+$ is not based solely on TD-DFT computations, which can suffer from well-documented defects including calculated transition energies in error by ∼5 000 cm^{-1} and CT transitions at unrealistically low energies,[67] these models were further compared on the basis of electronic transition energies using the multireference SORCI method.[69] Because of the computational demands of this method, SORCI calculations were performed on truncated species, where the mL_5^2 ligand was modeled by NH_3 groups. These models are referred to as $[Mn^{III}(O_2)(NH_3)_4\text{-N(4)}]^+$ and $[Mn^{III}(O_2)(NH_3)_4\text{-N(3)}]^+$. The consequences of this truncation were evaluated by comparing TD-DFT-computed Abs spectra of truncated models with those of authentic systems. As shown in Supporting Information, Figure S8, this truncation results in (i) a drop in absorption intensity, especially in the near-UV region, and (ii) a blue-shift of the electronic transition energies. Thus, in using SORCI computations to evaluate these models, we will only compare the computed electronic transition energies. The Abs spectra afforded from these calculations (Figure 9) provide further validation for the $[Mn^{III}(O_2)(mL_5^2)\text{-N(3)}]^+$ model as an accurate representation of $[Mn^{III}(O_2)(mL_5^2)]^+$. Indeed, considering the expected blue-shift and loss of Abs intensity for higher-energy transitions, the SORCI-computed Abs spectrum of $[Mn^{III}(O_2)(mL_5^2)\text{-N(3)}]^+$ is in remarkable agreement with experimental data. For example, the lowest-energy d-d transition of $[Mn^{III}(O_2)(NH_3)_4\text{-N(3)}]^+$ (band *iii*) is predicted at 18 172 cm^{-1} (*xy*-polarized), in good agreement with the position and polarization of band 1 (Figure 5 and Supporting Information, Table S15). In addition, the SORCI computations predict a set of two d-d and three peroxo-to-Mn^{III} CT transitions from 23 300−27 000 cm^{-1}

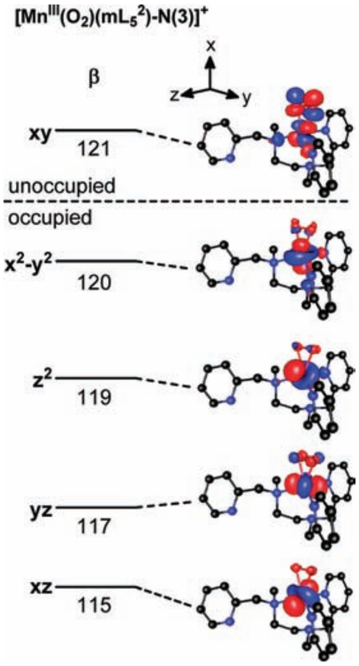

Figure 10. Schematic molecular orbital splitting diagram for [Mn^{III}(O$_2$)(mL$_5$^{2})-N(3)]$^+$ and surface contour plots of quasi-restricted orbitals based on DFT computations.

(band *iv*), in excellent agreement with the Gaussian deconvolution of the Abs and MCD data sets, which show a set of at least three bands in this spectral window (Figure 5). In contrast, the lowest-energy band for [Mn^{III}(O$_2$)(NH$_3$)$_4$-N(4)]$^+$ is centered at ~22 000 cm^{-1} (band *i*) and contains contributions from two transitions, a peroxo-to-manganese(III) CT transition at 21 589 cm^{-1} and a Mn^{III} d-d transition at 22 225 cm^{-1}, in poor agreement with the experimental data that show one band at ~17 000 cm^{-1}.

Given the success of the TD-DFT and SORCI computations for [Mn^{III}(O$_2$)(mL$_5$^{2})-N(3)]$^+$ in reproducing the major spectral features of [Mn^{III}(O$_2$)(mL$_5$^{2})]$^+$, it is warranted to discuss similarities and differences in the bonding descriptions provided by these methods and make spectral assignments. The Mn^{III} 3d splitting pattern afforded by the DFT computations is shown in Figure 10. The compositions of the spin-up Mn 3d-based Kohn–Sham MOs are in Table 4, and more complete information is provided in Supporting Information, Table S16. Because of the trigonal arrangement of the equatorial nitrogen donors, the Mn 3d-based MOs are mixtures of the canonical 3d orbitals, and are labeled according to the dominant contributor. For example, MO 120β is labeled as x^2-y^2, but this orbital contains significant contributions from x^2-y^2 (33%), xy (19%), z^2 (10%), and xz (10%). Because of this mixing, the surface contour plot of this MO only slightly resembles a canonical x^2-y^2 orbital (Figure 10). The lowest-energy Mn d-based MOs (xz and yz), which are both singly occupied, are involved in π-antibonding interactions with the peroxo ligand, as evidenced by the ~17% peroxo character in the spin-up MOs (MOs 105α and 109α in Table 4). The greater contributions from the mL$_5$^{2} ligand in the yz MO shift it to higher energy relative to xz. The singly occupied z^2 and x^2-y^2 MOs are predominantly involved in σ-antibonding interactions with the mL$_5$^{2} ligand, with the x^2-y^2 MO carrying more peroxo character than z^2 (11 versus 5%, respectively). The highest-energy Mn d-based MO (xy) is unoccupied and is the dominant Mn–O$_2$ σ-antibonding MO, containing similar contributions from Mn 3d and peroxo in-plane π^* MOs (π_{ip}*).[70] This electronic structure description of a high-spin (S = 2) Mn^{III} center and a peroxo (O$_2$$^{2-}$) ligand is largely consistent with that afforded by the multireference SORCI computations (Supporting Information, Table S17), where the leading (70%) configuration in the ground-state is $(\pi_{ip}^*)^2(\pi_{op}^*)^2(xz)^1(yz)^1(z^2)^1(x^2-y^2)^1(xy)^0$. However, this state contains an appreciable (10%) contribution from a $(\pi_{ip}^*)^1(\pi_{op}^*)^2(xz)^1(yz)^1(z^2)^1(x^2-y^2)^1(xy)^1$ configuration, which would formally be described as a high-spin (S = 5/2) Mn^{II} center antiferromagnetically coupled to a superoxo ligand (S = 1/2) to give S_{tot} = 2. Thus, this system is best described as a peroxomanganese(III) species, with very minor superoxomanganese(II) character in the ground-state wave function.

Table 4. Energies (eV) and Compositions of the Spin-Up (α) Mn 3d-based MOs from B3LYP Spin-Unrestricted DFT Computations for [Mn^{III}(O$_2$)(mL$_5$^{2})]$^+$

	xz (105α)	*yz* (109α)	*z*^{2} (110α)	*x*^{2}−*y*^{2} (113α)	*xy* (115α)
energy	−10.855	−10.221	−9.836	−9.014	−4.842
Mn 3d	57.3	33.0	24.9	39.2	30.7
z^2	5.9	1.1	13.3	12	0.3
x^2-y^2	39.5	1.1	8.6	1.9	0.1
xy	0.4	25.8	0.5	0.3	1.7
xz	9.9	2.2	1.1	14.5	9.8
yz	1.6	2.8	1.4	10.5	18.8
O$_2$ 2p	16.5	17.3	5.1	11.3	48.3
mL$_5$^{2} (N 2p)	7.3	24.5	38.9	32.8	5.9

According to the TD-DFT calculations, the lowest-energy d-d transition involves excitation from x^2-y^2 to xy, which is predicted at 18 015 cm^{-1} (band *i* in Figure 8, bottom), in good agreement with the experimental energy of band 1 (Table 1). In agreement, the lowest-energy SORCI-computed transition at 18 172 cm^{-1} (band *iii* in Figure 9, bottom) is due to an $x^2-y^2 \rightarrow xy$ one-electron excitation (Supporting Information, Table S17). At higher-energy, both the TD-DFT and SORCI methods predict an Abs band centered at ~23 000–25 000 cm^{-1} that contains contributions from a cluster of transitions, including peroxo-to-manganese(III) charge transfer bands, of which the O$_2$ $\pi_{op}^* \rightarrow yz$ is predicted as the most intense by both methods, and two d-d transitions ($z^2 \rightarrow xy$ and $yz \rightarrow xy$). Thus, these two computational methods are both in good agreement with our Gaussian analysis of Abs and MCD data collected for [Mn^{III}(O$_2$)(mL$_5$^{2})]$^+$.

2.3. Hypothetical Structures for [Mn^{III}(O$_2$)(imL$_5$^{2})]$^+$ and [Mn^{III}(O$_2$)(N4py)]$^+$. The spectroscopic similarities of [Mn^{III}(O$_2$)(mL$_5$^{2})]$^+$ with [Mn^{III}(O$_2$)(imL$_5$^{2})]$^+$ and [Mn^{III}(O$_2$)(N4py)]$^+$ require that these three complexes have similar geometries. DFT geometry optimizations of hypothetical models of [Mn^{III}(O$_2$)(imL$_5$^{2})]$^+$ and [Mn^{III}(O$_2$)(N4py)]$^+$ provide compelling evidence that ligand dissociation, resulting in the formation of six-coordinate Mn^{III} centers with side-on peroxo ligands, is energetically feasible for these systems as well (Table 3 and Figure 11). For [Mn^{III}(O$_2$)(imL$_5$^{2})]$^+$, dissociation of an imidazole arm in models [Mn^{III}(O$_2$)(imL$_5$^{2})-N(4)]$^+$ and [Mn^{III}(O$_2$)(imL$_5$^{2})-N(3)]$^+$ leads to significantly lower energies (~10–20 kcal/mol) relative to a model with a dissociated amine nitrogen *trans* to the peroxo group ([Mn^{III}(O$_2$)(imL$_5$^{2})-N(1)]$^+$). The structure of [Mn^{III}(O$_2$)(imL$_5$^{2})-N(3)]$^+$ is virtually identical to that of [Mn^{III}(O$_2$)(mL$_5$^{2})-N(3)]$^+$, consisting of an amine nitrogen *trans* to the

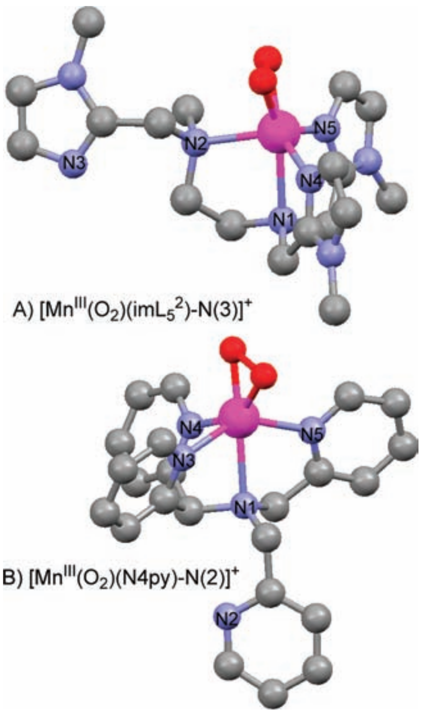

Figure 11. Molecular structures of [Mn^{III}(O$_2$)(imL$_5$^{2})-N(3)]$^+$ and [Mn^{III}(O$_2$)(N4py)-N(2)]$^+$ developed using DFT computations.

peroxo unit and three equatorial nitrogen donors (cf. Figure 11, top and Figure 7, bottom), and it is lower in energy than the [Mn^{III}(O$_2$)(imL$_5$^{2})-N(4)]$^+$ model by nearly 10 kcal/mol. While the Mn−N(1) distance is quite long in [Mn^{III}(O$_2$)(imL$_5$^{2})-N(3)]$^+$ (2.72 Å; see Table 3), shortening this bond to 2.40 Å is associated with an increase in energy of only 2.6 kcal/mol (Supporting Information, Table S18 and Figure S9, top). Consequently, the long Mn−N(1) distance might be exaggerated in the energy-minimized structure. In the TD-DFT-computed Abs spectra, shortening the Mn−N(1) distance leads to a red-shift of the lowest-energy Abs band (Supporting Information, Figure S9, bottom), lending credence to our proposal that the temperature-dependence of the experimental Abs spectrum of [Mn^{III}(O$_2$)(imL$_5$^{2})]$^+$ (Figure 4) is due to small, temperature-dependent changes in metal−ligand distances. For [Mn^{III}(O$_2$)(N4py)]$^+$, pyridine dissociation is also favored by ~20−25 kcal/mol (Table 3). The lowest-energy conformer, [Mn^{III}(O$_2$)(N4py)-N(2)]$^+$ (Figure 11, bottom), is structurally similar to [Mn^{III}(O$_2$)(mL$_5$^{2})-N(3)]$^+$ and [Mn^{III}(O$_2$)(imL$_5$^{2})-N(3)]$^+$, and the TD-DFT-computed Abs spectrum of this model is fully consistent with experimental data (Supporting Information, Figure S10).

■ DISCUSSION

While pentadentate ligands are often used to support peroxometal intermediates, including manganese[26,27] and iron[71−74] species, the molecular structures of these species have remained elusive. For example, while there are several crystallographically characterized peroxomanganese(III) adducts supported by tetradentate[20,23,24] and tridentate[21,22] ligands, corresponding adducts featuring pentadentate ligands are comparatively scarce and structural data is lacking for these species.[26,27] This is despite the fact that such pentadentate frameworks may provide higher fidelity to the first coordination spheres of Mn enzymes that react with oxygen and its reduced derivatives, as these often consist of five, tightly bound ligands (see Figure 1).[2,8,75] In this study, we have used a variety of spectroscopic and computational methods to demonstrate that the peroxomanganese(III) adducts supported by the pentadentate mL$_5$^{2}, imL$_5$^{2}, and N4py ligands feature six-coordinate Mn^{III} centers with side-on peroxo ligands, which requires the ligands convert from a pentadentate binding mode in the Mn^{II} complexes to a tetradentate mode for the Mn^{III}−O$_2$ species. Specifically, on the basis of DFT-computed energies and the agreement between experimental and calculated spectroscopic data, we conclude that these six-coordinate, side-on peroxomanganese(III) complexes feature pyridine (or imidazole) arms that are dissociated. The implications of these studies for biological Mn enzymes, related peroxometal adducts, and peroxomanganese(III) decay pathways are discussed below.

Relevance to Catalytic Manganese Centers in Biological and Synthetic Systems. Dissociation of a pyridine or imidazole arm for the mL$_5$^{2}, imL$_5$^{2}, and N4py ligands is possible in the peroxomanganese(III) complexes because these ligands can adopt a variety of metal-binding modes, some of which are of comparable energy. This is illustrated in the three hypothetical structures developed for [Mn^{III}(O$_2$)(mL$_5$^{2})]$^+$ (Figure 7). In contrast to these apparently flexible pentadentate ligands, metalloenzyme active sites, such as those of MnSOD and MndD (Figure 1), typically feature amino acid ligands whose positions are greatly constrained by the protein matrix. In these systems ligand dissociation would presumably be disfavored energetically. By limiting the coordination sites available for peroxo (or superoxo) binding, these sites may inhibit the formation of more thermodynamically stable side-on peroxomanganese(III) centers.[3] Surface scans evaluating the conversion from side-on to end-on peroxo binding for [Mn^{III}(O$_2$)(mL$_5$^{2})]$^+$ revealed an inverse correlation between one Mn−O$_{peroxo}$ distance and the Mn−N(1) distance, where the N(1) ligand is *trans* to the peroxo unit. On the basis of this correlation, a short, strong Mn−L bond *trans* to the peroxo unit would favor end-on peroxo binding. In the case of [Mn^{III}(O$_2$)(mL$_5$^{2})]$^+$, shorter Mn−N(1) and longer Mn−O$_{peroxo}$ distances led to a thermodynamic destabilization, because strengthening the Mn−N(1) bond could not compensate for weakening the Mn−O$_{peroxo}$ bond. However, it is speculated that a stronger *trans* ligand (e.g., a carboxylate) could make side-on and end-on peroxo binding modes comparable in energy. This model is consistent with the proposal by Nam and co-workers that anionic *trans* ligands in [Mn^{III}(O$_2$)(13-TMC)(X)] could elongate one Mn−O$_{peroxo}$ bond, thus leading to the observed increase in reactivity upon X$^-$ binding.[23] In addition, according to this model, the presence of a carboxylate ligand *trans* to the expected superoxide and dioxygen binding sites in MnSOD and MndD, respectively, would further disfavor side-on binding in these active sites.[3]

The proposal that pyridine and imidazole dissociation is possible for the mL$_5$^{2}, imL$_5$^{2}, and N4py ligands also has relevance for metal-catalyzed transformations that utilize these types of pentadentate ligands. Such ligands are employed in catalytic reactions including textile and wood pulp bleaching, a variety of substrate oxygenation reactions, and atom transfer radical polymerizations.[76−81] On the basis of our results, it may not be well-founded to assume that such ligands remain bound in a pentadentate mode during catalysis.

Comparison to Peroxoiron(III) Adducts. The mL$_5$^{2} and N4py ligands have been previously used to support high-spin peroxoiron(III) complexes.[74,82,83] While there is consensus that these species contain side-on peroxo ligands, it is unclear as to whether the ligands are bound in a pentadentate or tetradentate fashion, which would respectively give rise to seven- and six-coordinate ferric centers.[73,74,82−84] While our data supports tetradentate ligand binding for the peroxomanganese(III) complexes of the mL_5^2 and N4py ligands, one should take caution in transferring this conclusion to the corresponding peroxoiron(III) systems. One contrast between these systems are the significantly longer $Fe-O_{peroxo}$ distances, which, on the basis of iron K-edge extended X-ray absorption fine structure (EXAFS) data and DFT computations, range from 1.91 to 1.99 Å.[73,74,85] These distances are roughly 0.05−0.1 Å longer than $Mn-O_{peroxo}$ bond lengths observed by X-ray crystallography.[20−24] For an even comparison, $M-O_{peroxo}$ distances calculated for seven-coordinate models of $[Fe^{III}(O_2)(N4py)]^+$ and $[Mn^{III}(O_2)(N4py)]^+$ are 1.96[74] and 1.87 Å, respectively. This relatively large difference in bond length can be attributed to the different electronic configurations of $Fe^{III}-O_2$ and $Mn^{III}-O_2$ species. For the high-spin d^5 $Fe^{III}-O_2$ species, the $Fe-O_2$ σ*-based MO, which consists of interactions between a metal d_σ orbital (typically d_{xy}) and the in-plane peroxo π-antibonding orbital (O_2 π_{ip}*), is singly occupied.[86,87] For the corresponding high-spin, d^4 $Mn^{III}-O_2$ system, this orbital is unoccupied (Figure 10),[29] which leads to a strengthening and shortening of the metal-peroxo bond. This difference in $M-O_2$ σ*-orbital occupancy is likely responsible for the higher O−O stretching frequencies (ν_{O-O}) observed for the $Mn^{III}-O_2$ adducts, which are blue-shifted by ~70 cm^{-1} compared to those of high-spin $Fe^{III}-O_2$ complexes. The O−O bond is strengthened by the admixture of more O_2 π_{ip}* character into the unoccupied $Mn-O_2$ σ*-based MO.

To assess the effect of these different electronic configurations on the coordination preferences of peroxoiron(III) and peroxomanganese(III) species, we used DFT computations to develop models of $[Fe^{III}(O_2)(mL_5^2)]^+$ analogous to those of $[Mn^{III}(O_2)(mL_5^2)]^+$. The change in metal has a dramatic effect on the relative energies of the three isomers, as shown in Figure 12 (top). For $[Fe^{III}(O_2)(mL_5^2)]^+$ the lowest energy isomer has a seven-coordinate ferric center with no pyridine arms dissociated (referred to as $[Fe^{III}(O_2)(mL_5^2)\text{-}N(1)]^+$; Figure 12, bottom), in complete contrast to that observed for $[Mn^{III}(O_2)(mL_5^2)]^+$. The optimized $[Fe^{III}(O_2)(mL_5^2)\text{-}N(1)]^+$ complex has $Fe-O_{peroxo}$ bond lengths of 1.99 and 2.00 Å (Supporting Information, Table S19), significantly longer than in the correspond $Mn-O_2$ species (1.899 and 1.894 Å; see Table 3). The Fe−N(1) distance is long, but still near a bond distance for a high-spin ferric center. Taken together, these results strongly suggest that peroxoiron(III) and peroxomanganese(III) adducts have very different preferences with regards to coordination geometry, which is expected to have mechanistic implications for biological and synthetic catalysts.

Acid-Assisted Decay Pathway of $[Mn^{III}(O_2)(mL_5^2)]^+$. In the presence of acid, the decay pathway of $[Mn^{III}(O_2)(mL_5^2)]^+$ involves ligand oxidation, where 2-pyridinecarboxylate is generated by oxidative cleavage of a pyridine arm from the mL_5^2 ligand.[27] This observed decay product is suggestive of acid-assisted O−O bond activation to create an oxomanganese species (either Mn^{IV} or Mn^V, depending on whether O−O cleavage occurs by a homolytic or heterolytic pathway). Such behavior has recently been observed for nonheme peroxoiron(III) and peroxomanganese(IV) corrole species, which respectively convert to oxoiron(IV) and oxomanganese(V) adducts when treated with acid.[88,89] However, there is growing evidence that, under certain circumstances, hydroperoxometal species are capable of acting as H-atom abstraction agents,[90,91] initiating oxidation reactions. Thus for the present system it is unclear whether an oxo- or hydroperoxomanganese species is responsible for the observed chemistry. Regardless of the nature of the active oxidant in this process, there is currently no experimental data available to provide insight into whether this decay pathway involves inter- or intramolecular ligand oxidation. The geometric structure of $[Mn^{III}(O_2)(mL_5^2)\text{-}N(3)]^+$ (Figure 7, bottom) lends credence to an intramolecular pathway, as the orientation of the methyl linker in the dissociated pyridine appears well positioned for intramolecular attack by a Mn=O (or Mn-OOH) species ($H-O_{peroxo}$ distance of 2.6 Å in $[Mn^{III}(O_2)(mL_5^2)\text{-}N(3)]^+$). Alternatively, hydroxyl radicals formed by acid-assisted O−O homolysis could be responsible for ligand oxidation. Determining the nature of the active oxidant as well as the details of this ligand degradation pathway, would not only aid in understanding O−O bond activation in Mn systems, but also could provide insights into the design of more robust ligands for use in catalytic oxidation reactions.

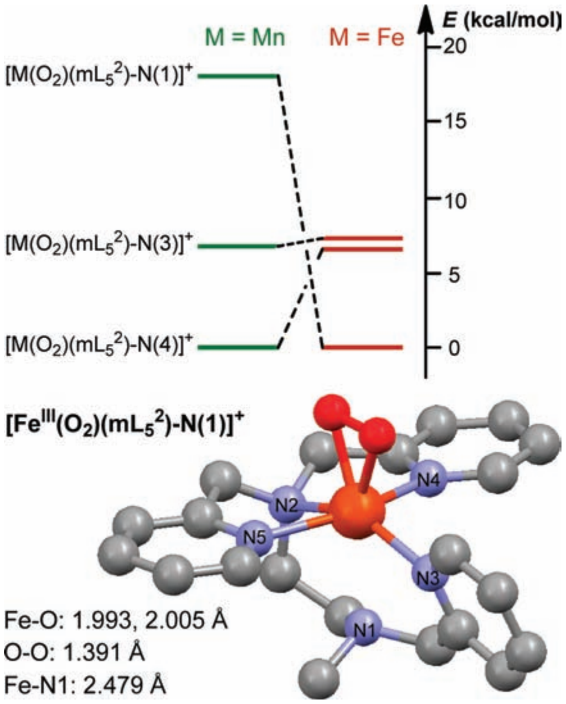

Figure 12. Top: Relative energies of $[M^{III}(O_2)(mL_5^2)\text{-}N(1)]^+$, $[M^{III}(O_2)(mL_5^2)\text{-}N(3)]^+$, and $[M^{III}(O_2)(mL_5^2)\text{-}N(4)]^+$ isomers (left: M = Mn and right: M = Fe). For each metal, the energies are plotted relative to the lowest-energy isomer. Bottom: DFT-optimized structure of $[Fe^{III}(O_2)(mL_5^2)\text{-}N(1)]^{+s}$, with Fe−O, O−O, and Fe−N(1) distances indicated.

■ ASSOCIATED CONTENT

Ⓢ Supporting Information. Cartesian coordinates for all DFT-optimized models, detailed parameters used in fitting absorption, MCD, and VTVH MCD data, the results of DFT surface scans, germane output from TD-DFT and SORCI computations, and VTVH MCD contour plots. This material is available free of charge via the Internet at http://pubs.acs.org.

AUTHOR INFORMATION

Corresponding Authors

*Phone: (785) 864-3968 (T.A.J.), + 33 (0)1 57 27 87 84 (E.A.-M.). Fax: (785) 864-5396 (T.A.J.). E-mail: taj@ku.edu (T.A.J.), elodie.anxolabehere@univ-paris-diderot.fr (E.A.-M.).

Present Addresses

[‖] Department of Chemistry, Kalyani University, West Bengal, India

ACKNOWLEDGMENT

T.A.J. acknowledges the University of Kansas, the Center for Environmentally Beneficial Catalysis (Lawrence, KS), and the American Chemical Society Petroleum Research Fund (50287-DNI3) for support. E.A.-M. acknowledges ANR TAKE-CARE for financial support.

REFERENCES

(1) Grove, L. E.; Brunold, T. C. *Comments Inorg. Chem.* **2008**, *29*, 134–168.

(2) Miller, A.-F. *Curr. Opin. Chem. Biol.* **2004**, *8*, 162–168.

(3) Jackson, T. A.; Karapetian, A.; Miller, A.-F.; Brunold, T. C. *Biochemistry* **2005**, *44*, 1504–1520.

(4) Bull, C.; Niederhoffer, E. C.; Yoshida, T.; Fee, J. A. *J. Am. Chem. Soc.* **1991**, *113*, 4069–4076.

(5) Hearn, A. S.; Stroupe, M. E.; Cabelli, D. E.; Lepock, J. R.; Tainer, J. A.; Nick, H. S.; Silverman, D. N. *Biochemistry* **2001**, *40*, 12051–12058.

(6) Hearn, A. S.; Tu, C. K.; Nick, H. S.; Silverman, D. N. *J. Biol. Chem.* **1999**, *274*, 24457–24460.

(7) Gunderson, W. A.; Zatsman, A. I.; Emerson, J. P.; Farquhar, E. R.; Que, L.; Lipscomb, J. D.; Hendrich, M. P. *J. Am. Chem. Soc.* **2008**, *130*, 14465–14467.

(8) Vetting, M. W.; Wackett, L. P.; Que, L., Jr.; Lipscomb, J. D.; Ohlendorf, D. H. *J. Bacteriol.* **2004**, *186*, 1945–1958.

(9) Opaleye, O.; Rose, R.-S.; Whittaker, M. M.; Woo, E.-J.; Whittaker, J. W.; Pickersgill, R. W. *J. Biol. Chem.* **2006**, *281*, 6428–6433.

(10) Borowski, T.; Bassan, A.; Richards, N. G. J.; Siegbahn, P. E. M. *J. Chem. Theory Comput.* **2005**, *1*, 686–693.

(11) Reinhardt, L. A.; Svedruzic, D.; Chang, C. H.; Cleland, W. W.; Richards, N. G. J. *J. Am. Chem. Soc.* **2003**, *125*, 1244–1252.

(12) Svedružic, D.; Jónsoon, S.; Toyota, C. G.; Reinhardt, L. A.; Ricagno, S.; Lindqvist, Y.; Richards, N. G. J. *Arch. Biochem. Biophys.* **2005**, *433*, 176–192.

(13) Tanner, A.; Bowater, L.; Fairhurst, S. A.; Bornemann, S. *J. Biol. Chem.* **2001**, *276*, 43627–43634.

(14) Wu, A. J.; Penner-Hahn, J. E.; Pecoraro, V. L. *Chem. Rev.* **2004**, *104*, 903–938.

(15) Cotruvo, J. A.; Stubbe, J. *Biochemistry* **2010**, *49*, 1297–1309.

(16) Hearn, A. S.; Stroupe, M. E.; Cabelli, D. E.; Ramilo, C. A.; Luba, J. P.; Tainer, J. A.; Nick, H. S.; Silverman, D. N. *Biochemistry* **2003**, *42*, 2781–2789.

(17) Guan, Y.; Hickey, M. J.; Borgstahl, G. E. O.; Hallewell, R. A.; Lepock, J. R.; O'Connor, D.; Hsieh, Y. S.; Nick, H. S.; Silverman, D. N.; Tainer, J. A. *Biochemistry* **1998**, *37*, 4722–4730.

(18) Hsieh, Y. S.; Guan, Y.; Tu, C. K.; Bratt, P. J.; Angerhofer, A.; Lepock, J. R.; Hickey, M. J.; Tainer, J. A.; Nick, H. S.; Silverman, D. N. *Biochemistry* **1998**, *37*, 4731–4739.

(19) Lévêque, V. J.-P.; Stroupe, M. E.; Lepock, J. R.; Cabelli, D. E.; Tainer, J. A.; Nick, H. S.; Silverman, D. N. *Biochemistry* **2000**, *39*, 7131–7137.

(20) VanAtta, R. B.; Strouse, C. E.; Hanson, L. K.; Valentine, J. S. *J. Am. Chem. Soc.* **1987**, *109*, 1425–1434.

(21) Kitajima, N.; Komatsuzaki, H.; Hikichi, S.; Osawa, M.; Moro-oka, Y. *J. Am. Chem. Soc.* **1994**, *116*, 11596–11597.

(22) Singh, U. P.; Sharma, A. K.; Hikichi, S.; Komatsuzaki, H.; Moro-oka, Y.; Akita, M. *Inorg. Chim. Acta* **2006**, *359*, 4407–4411.

(23) Annaraj, J.; Cho, J.; Lee, Y.-M.; Kim, S. Y.; Latifi, R.; de Visser, S. P.; Nam, W. *Angew. Chem., Int. Ed.* **2009**, *48*, 4150–4153.

(24) Seo, M. S.; Kim, J. Y.; Annaraj, J.; Kim, Y.; Lee, Y.-M.; Kim, S.-J.; Kim, J.; Nam, W. *Angew. Chem., Int. Ed.* **2007**, *46*, 377–380.

(25) Grapperhaus, C. A.; Mienert, B.; Bill, E.; Weyhermuller, T.; Wieghardt, K. *Inorg. Chem.* **2000**, *39*, 5306–5317.

(26) Groni, S.; Blain, G.; Guillot, R.; Policar, C.; Anxolabéhère-Mallart, E. *Inorg. Chem.* **2007**, *46*, 1951–1953.

(27) Groni, S.; Dorlet, P.; Blain, G.; Bourcier, S.; Guillot, R.; Anxolabéhère-Mallart, E. *Inorg. Chem.* **2008**, *47*, 3166–3172.

(28) Shook, R. L.; Gunderson, W. A.; Greaves, J.; Ziller, J. W.; Hendrich, M. P.; Borovik, A. S. *J. Am. Chem. Soc.* **2008**, *130*, 8888–8889.

(29) Geiger, R. A.; Chattopadhyay, S.; Day, V. W.; Jackson, T. A. *J. Am. Chem. Soc.* **2010**, *132*, 2821–2831.

(30) Shook, R. L.; Borovik, A. S. *Inorg. Chem.* **2010**, *49*, 3646–3660.

(31) Geiger, R. A.; Chattopadhyay, S.; Day, V. W.; Jackson, T. A. *Dalton Trans.* **2011**, *40*, 1707–1715.

(32) Emerson, J. P.; Kovaleva, E. G.; Farquhar, E. R.; Lipscomb, J. D.; Que, L., Jr. *Proc. Natl. Acad. Sci. U.S.A.* **2008**, *105*, 7347–7352.

(33) Wei, N.; Murthy, N. N.; Tyeklar, Z.; Karlin, K. D. *Inorg. Chem.* **1994**, *33*, 1177–1183.

(34) Pascaly, M.; Duda, M.; Rompel, A.; Sift, B. H.; Meyer-Klaucke, W.; Krebs, B. *Inorg. Chim. Acta* **1999**, *291*, 289–299.

(35) Chang, J.; Plummer, S.; Berman, E. S. F.; Striplin, D.; Blauch, D. *Inorg. Chem.* **2004**, *43*, 1735–1742.

(36) Lubben, M.; Meetsma, A.; Wilkinson, E. C.; Feringa, B.; Que, L., Jr. *Angew. Chem., Int. Ed.* **1995**, *34*, 1512–1514.

(37) Hurea, C.; Groni, S.; Guillot, R.; Blondin, G.; Duboc, C.; Anxolabéhère-Mallart, E. *Inorg. Chem.* **2008**, *47*, 9238–9247.

(38) Neese, F. *ORCA - an ab initio, Density Functional and Semiempirical Program Package*, Version 2.8; University of Bonn: Bonn, Germany, 2009.

(39) Becke, A. D. *J. Chem. Phys.* **1986**, *84*, 4524–4529.

(40) Perdew, J. P. *Phys. Rev. B* **1986**, *33*, 8822–8824.

(41) Schäfer, A.; Horn, H.; Ahlrichs, R. *J. Chem. Phys.* **1992**, *97*, 2571–2577.

(42) Schäfer, G.; Huber, C.; Ahlrichs, R. *J. Chem. Phys.* **1994**, *100*, 5829–5835.

(43) Neese, F. *J. Comput. Chem.* **2003**, *24*, 1740–1747.

(44) Becke, A. D. *J. Chem. Phys.* **1993**, *98*, 1372–1377.

(45) Becke, A. D. *J. Chem. Phys.* **1993**, *98*, 5648–5652.

(46) Lee, C.; Yang, W.; Parr, R. G. *Phys. Rev. B* **1988**, *37*, 785–789.

(47) Weigend, F.; Ahlrichs, R. *Phys. Chem. Chem. Phys.* **2005**, *7*, 3297–3305.

(48) Neese, F. *J. Chem. Phys.* **2007**, *127*, 164112–164119.

(49) Bergman, D. L.; Laaksonen, L.; Laaksonen, A. *J. Mol. Graphics Modell.* **1997**, *15*, 301–306.

(50) Laaksonen, L. *J. Mol. Graphics* **1992**, *10*, 33–34.

(51) Bauernschmitt, R.; Ahlrichs, R. *Chem. Phys. Lett.* **1996**, *256*, 454–464.

(52) Casida, E. M.; Jamorski, C.; Casida, K. C.; Salahub, D. R. *J. Chem. Phys.* **1998**, *108*, 4439–4449.

(53) Stratman, R. E.; Scuseria, G. E.; Frisch, M. J. *J. Chem. Phys.* **1998**, *109*, 8218–8224.

(54) Neese, F.; Olbrich, G. *Chem. Phys. Lett.* **2002**, *362*, 170–178.

(55) Neese, F.; Petrenko, T.; Ganyushin, D.; Olbrich, G. *Coord. Chem. Rev.* **2007**, *205*, 288.

(56) Neese, F. *J. Inorg. Biochem.* **2006**, *100*, 716–726.

(57) Lassalle-Kaiser, B.; Ghachtouli, S. E.; Guillot, R.; Leto, D. F.; Chattopadhyay, S.; Day, V. W.; Jackson, T. A.; Dorlet, P.; Anxolabéhère-Mallart, E., unpublished results.

(58) Unlike the $[Mn^{II}(mL_5{}^2)]^{2+}$ and $[Mn^{II}(imL_5{}^2)]^{2+}$ complexes that yield Mn^{III}-O_2 adducts upon treatment with either KO_2 or H_2O_2/Et_3N at low temperature, the addition of H_2O_2/Et_3N to $[Mn^{II}(N4py)]^{2+}$ results in the formation of the oxo-bridged dimer $[Mn^{III}Mn^{IV}(\mu\text{-}O_2)(N4py)_2]^{3+}$.

(59) All extinction coefficients were determined under the assumption that 100% of Mn^{II} is converted to the corresponding peroxomanganese(III)

species. Because it has been reported that the reaction of $[\mathrm{Mn^{II}}(\mathrm{mL_5}^{2})]^{+}$ with hydrogen peroxide results in some unreacted $\mathrm{Mn^{II}}$, the extinction coefficients should be viewed as a lower limit. However, with these ligand sets, any $\mathrm{Mn^{II}}$ species present in solution will not contribute to the absorption or MCD spectra in the visible and near-UV regions. Thus, these experiments selectively probe the $\mathrm{Mn^{III}}$ complexes.

(60) Whittaker, M. M.; Whittaker, J. W. *Biochemistry* **1996**, *35*, 6762–6770.

(61) Kirk, M. L.; Peariso, K. *Curr. Opin. Chem. Biol.* **2003**, *7*, 220–227.

(62) Neese, F.; Solomon, E. I. *Inorg. Chem.* **1999**, *38*, 1847–1865.

(63) Despite numerous attempts, we were unable to acceptably fit VTVH MCD data collected for $[\mathrm{Mn^{III}}(\mathrm{O_2})(\mathrm{N4py})]^{+}$ at higher energies. We presume this is due to the overlap of electronic transitions with different polarizations at higher energies. Alternatively, larger MCD *B*-term contributions could also affect the quality of VTVH MCD data collected at these wavelengths.

(64) Nivorozhkin, A. L.; Anxolabéhère-Mallart, E.; Mialane, P.; Davydov, R.; Guilhem, J.; Cesario, M.; Audière, J.-P.; Girerd, J.-J.; Styring, S.; Schussler, L.; Seris, J.-L. *Inorg. Chem.* **1997**, *36*, 846–853.

(65) bpmg = 2-[[2-[bis(pyridin-2-ylmethyl)amino]-ethyl](methyl)-amino]acetic acid and mcbpen = *N*-methyl-*N*′-carboxymethyl-*N*,*N*′-bis-(pyridylmethyl)ethane-1,2-diamine.

(66) Berggren, G.; Thapper, A.; Huang, P.; Eriksson, L.; Styring, S. r.; Anderlund, M. F. *Inorg. Chem.* **2011**, *50*, 3425–3430.

(67) Neese, F. *J. Biol. Inorg. Chem.* **2006**, *11*, 702–711.

(68) The TD-DFT-computed transition polarizations are relative to the principal axes of the *D*-tensor, as determined by coupled-perturbed DFT computations.

(69) Neese, F. *J. Chem. Phys.* **2003**, *119*, 9428–9443.

(70) The peroxo frontier orbitals, which are O—O π-antibonding, are conventionally classified as in-plane (π_{ip}*) or out-of-plane (π_{op}*) depending on their orientation with respect to the metal-peroxo bond vectors.

(71) Costas, M.; Mehn, M. P.; Jensen, M. P.; Que, L., Jr. *Chem. Rev.* **2004**, *104*, 939–986.

(72) Girerd, J.-J.; Banse, F.; Simaan, A. J. *Struct. Bonding* **2000**, *97*, 143–177.

(73) Koehntop, K. D.; Rohde, J.-U.; Costas, M.; Que, L., Jr *Dalton Trans.* **2004**, 3191–3198.

(74) Roelfes, G.; Vrajmasu, V.; Chen, K.; Ho, R. Y. N.; Rohde, J.-U.; Zondervan, C.; la Crois, R. M.; Schudde, E. P.; Lutz, M.; Spek, A. L.; Hage, R.; Feringa, B. L.; Münck, E.; Que, L. J. *Inorg. Chem.* **2003**, *42*, 2639–2653.

(75) Miller, A.-F., Superoxide processing. In *Comprehensive Coordination Chemistry II*; McCleverty, J. A., Meyer, T. J., Eds.; Elsevier Ltd.: Oxford, U.K., 2004; Vol. 8, pp 479—506.

(76) Klopstra, M.; Hage, R.; Kellogg, R. M.; Feringa, B. L. *Tetrahedron Lett.* **2003**, *44*, 4581–4584.

(77) Roelfes, G.; Lubben, M.; Hage, R.; Que, J. L.; Feringa, B. L. *Chem.—Eur. J.* **2000**, *6*, 2152–2159.

(78) Roelfes, G.; Lubben, M.; Leppard, S. W.; Schudde, E. P.; Hermant, R. M.; Hage, R.; Wilkinson, E. C.; Que, L.; Feringa, B. L. *J. Mol. Catal. A: Chem.* **1997**, *117*, 223–227.

(79) van den Berg, T. A.; de Boer, J. W.; Browne, W. R.; Roelfes, G.; Feringa, B. L. *Chem. Commun.* **2004**, 2550–2551.

(80) Zhang, L.; Tang, H.; Tang, J.; Shen, Y.; Meng, L.; Radosz, M.; Arulsamy, N. *Macromolecules* **2009**, *42*, 4531–4538.

(81) Hage, R.; Lienke, A. *Angew. Chem., Int. Ed.* **2006**, *45*, 206–222.

(82) Simaan, A. J.; Banse, F.; Mialane, P.; Boussac, A.; Un, S.; Kargar-Grisel, T.; Bouchoux, G.; Girerd, J.-J. *Eur. J. Inorg. Chem.* **1999**, 993–996.

(83) Simaan, A. J.; Döpner, S.; Banse, F.; Bourcier, S.; Bouchoux, G.; Boussac, A.; Hildebrandt, P.; Girerd, J.-J. *Eur. J. Inorg. Chem.* **2000**, 1627–1633.

(84) Hazell, A.; McKenzie, C. J.; Nielsen, L. P.; Schindler, S.; Weitzer, M. *J. Chem. Soc., Dalton Trans.* **2002**, 310–317.

(85) Bukowski, M. R.; Comba, P.; Limberg, C.; Merz, M.; Que, L.; Wistuba, T. *Angew. Chem., Int. Ed.* **2004**, *43*, 1283–1287.

(86) Neese, F.; Solomon, E. I. *J. Am. Chem. Soc.* **1998**, *120*, 12829–12848.

(87) Solomon, E. I.; Brunold, T. C.; Davis, M. I.; Kemsley, J. N.; Lee, S. K.; Lehnert, N.; Neese, F.; Skulan, A. J.; Yang, Y. S.; Zhou, J. *Chem. Rev.* **2000**, *100*, 235–349.

(88) Kim, S. H.; Park, H.; Seo, M. S.; Kubo, M.; Ogura, T.; Klajn, J.; Gryko, D. T.; Valentine, J. S.; Nam, W. *J. Am. Chem. Soc.* **2010**, *132*, 14030–14032.

(89) Li, F.; Meier, K. K.; Cranswick, M. A.; Chakrabarti, M.; Van Heuvelen, K. M.; Münck, E.; Que, L. *J. Am. Chem. Soc.* **2011**, *133*, 7256–27259.

(90) Decker, A.; Chow, M. S.; Kemsley, J. N.; Lehnert, N.; Solomon, E. I. *J. Am. Chem. Soc.* **2006**, *128*, 4719–4733.

(91) Liu, L. V.; Bell, C. B.; Wong, S. D.; Wilson, S. A.; Kwak, Y.; Chow, M. S.; Zhao, J.; Hodgson, K. O.; Hedman, B.; Solomon, E. I. *Proc. Natl. Acad. Sci.* **2010**, *107*, 22419–22424.